The Analogous Structure of Accretion Flows in Supermassive and Stellar Mass Black Holes

J. J. Ruan[1,2], S. F. Anderson[2], M. Eracleous[3], P. J. Green[4], D. Haggard[1,5], C. L. MacLeod[4], J. C. Runnoe[6] & M. A. Sobolewska[4]

[1]McGill Space Institute and Department of Physics, McGill University, 3600 rue University, Montréal, Québec H3A 2T8, Canada [2]Department of Astronomy, University of Washington, Box 351580, Seattle, WA 98195, USA [3]Department of Astronomy & Astrophysics and Institute for Gravitation and the Cosmos, The Pennsylvania State University, 525 Davey Lab, University Park, PA 16802, USA [4]Harvard Smithsonian Center for Astrophysics, 60 Garden St, Cambridge, MA 02138, USA [5]CIFAR Azrieli Global Scholar, Gravity & the Extreme Universe Program, Canadian Institute for Advanced Research, 661 University Avenue, Suite 505, Toronto, ON M5G 1M1, Canada [6]Department of Astronomy, University of Michigan, 1085 S. University Avenue, Ann Arbor, MI 48109, USA

Black holes grow rapidly through the accretion of gas. As the accretion rate onto a black hole decreases, the structure of its surrounding accretion flow is believed to dramatically transition from a luminous thin disc[1] to become quasi-spherical and radiatively inefficient[2]. These accretion state transitions are commonly observed for stellar mass black holes in Galactic X-ray binary systems[3], but it is unknown if this process occurs similarly for supermassive black holes at the centres of galaxies. Here, we show that the geometry of the accretion flow around supermassive and stellar mass black holes evolve analogously during transitions between different accretion states. We use X-ray and rest-UV observations of faded 'changing-look' quasars[4] to probe the geometry of the feeble accretion flows around their supermassive black holes, based on the spectral changes as a function of Eddington ratio. We find that the observed spectral evolution in fading quasars displays a remarkable similarity to accretion state transitions in X-ray binary outbursts. Our results show that the structures of black hole accretion flows directly scales across a factor of 10^8 in black hole mass, and enables us to apply theoretical models of X-ray binaries to explain active galactic nuclei phenomenology.

We observe black holes in two main types that are distinguished by their vastly different masses, although both types grow through the accretion of gas. Stellar mass black holes found in X-ray binary systems have typical masses of $\sim$5-10 $M_\odot$, and they are observed when the black hole accretes from a companion star. In contrast, supermassive black holes at the centres of galaxies have typical masses of $\sim 10^{7-9}$ $M_\odot$, and they are observed as active galactic nuclei (AGN) when they accrete from their nearby gas-rich environment. Based on observations of both X-ray binaries and AGN, it is now thought that the *structure* of accretion flows around both types of black holes depends primarily on the *rate* of accretion per unit black hole mass. As the accretion rate fluctuates, the accretion flow transitions dramatically into different states, each with distinct geometries and multi-wavelength spectral characteristics.

Direct observations of accretion state transitions in stellar mass black holes have revealed a rich phenomenology[3,5], that have lead to concordant physical models[6]. At high accretion rates, the accretion flow in X-ray binaries forms a geometrically-thin accretion disc[1] that emits luminous thermal soft X-rays; this accretion state is known as the high-luminosity/soft-spectrum state. As the accretion rate drops, the inner region of the thin disc may progressively truncate[7] and expand into a quasi-spherical radiatively inefficient accretion flow[2] that is possibly advection dominated[8], while hard X-rays from a compact corona above the disc dominate the overall emission. During this process, the X-ray spectrum is observed to harden, and the X-ray binary enters a low-luminosity/hard-spectrum state. At a bolometric Eddington ratio below $L_{\rm bol}/L_{\rm Edd} \lesssim 10^{-2}$ in the low/hard state, the X-ray spectrum is observed to soften again, likely due to the onset of an additional (e.g., synchrotron) emission component[9]. Despite the success of this general picture for accretion state transitions in stellar mass black holes, it is still unclear if supermassive black hole accretion flows undergo similar processes.

Previous observations have revealed evidence that AGNs display some characteristics of X-ray binary phenomenology, and interpretations of these similarities often propose that black hole accretion flows are scale-invariant[10–14]. This AGN/X-ray binary analogy asserts that AGN behave as X-ray binaries that are scaled-up in size, and thus will also transition through analogous accretion states in response to changes in their accretion rate. However, accretion state transitions in AGN have not been observed directly, likely because the timescale expected for this process also scales up with black hole mass, from a few days in X-ray binaries to possibly $\sim 10^{4-5}$ years in AGN. Thus, direct evidence for such an analogy in the underlying geometry of black hole accretion flows has remained observationally elusive.

To test whether the structure of accretion flows undergo similar state transitions in both stellar mass and supermassive black holes, we compare observations of prototypical accretion state transitions in an X-ray binary to a *sample* of AGN that spans a wide range of accretion rates. In X-ray binaries, the structure of the accretion flow may be probed using the X-ray spectral index, which changes during accretion state transitions due to the evolving geometry of the disc-corona system. For AGN, we can similarly probe the structure of the accretion flow using the UV-to-X-ray spectral index ($\alpha_{\rm OX}$) between 2500 Å and 2 keV, since the thin disc emission peaks in the UV and the coronal emission dominates the X-rays. Thus, our approach is to measure the $\alpha_{\rm OX}$ of a sample of AGN with a wide range of accretion rates, and compare these $\alpha_{\rm OX}$ values to the spectral behaviour of an X-ray binary undergoing an accretion state transition. We find that changes in AGN accretion rate correspond to spectral changes that are remarkably similar to those observed in X-ray binaries, suggesting that the structure of black hole accretion flows are indeed analogous.

The key to our novel approach is to include faded 'changing-look' quasars in our AGN sample, which enables us to extend measurements of $\alpha_{\rm OX}$ to low Eddington ratios ($L_{\rm bol}/L_{\rm Edd} \lesssim 10^{-2}$). Faded changing-look quasars are a class of AGN that are characterized by dramatic fading of their broad emission lines and continuum in repeat optical spectroscopy (see Fig. 1)[4,15–19]. We emphasize that we are *not* directly observing accretion state transitions in our changing-look quasars, since they fade from $L_{\rm bol}/L_{\rm Edd} \sim 10^{-1.5}$ to $\sim 10^{-3.5}$ and thus are already in the low/hard state even before their fading. Nevertheless, they are key to probing how $\alpha_{\rm OX}$ changes over a wide range of Eddington ratios for two primary reasons. Firstly, at low Eddington ratios, AGN are often dust obscured[20], and thus measuring their intrinsic UV luminosities is difficult. Since changing-look quasars are observed to be Type 1 AGN (i.e., unobscured) before their fading, and their fading have been shown to be consistent with a decrease in their accretion rate while disfavoring dust obscuration[4,15–19,21–24], we know that their

UV luminosities after they fade are also unobscured. Secondly, tracing how $\alpha_{\rm OX}$ changes as a function of Eddington ratio in AGN requires a sample of AGN with similar black hole masses ($M_{\rm BH}$), to avoid complications from the $T \propto M_{\rm BH}^{-1/4}$ scaling of the thin disc temperature with $M_{\rm BH}$ at a fixed Eddington ratio. However, $M_{\rm BH}$ is often difficult to measure for AGN at low luminosities, where broad emission lines disappear. Changing-look quasars allow us to bypass this problem, because we can use a sample of AGN with a narrow distribution of $M_{\rm BH}$ that is determined using the prominent broad emission lines in their optical spectra before they fade, and then measure their $\alpha_{\rm OX}$ at low accretion rates after they fade.

We use rest-frame UV and X-ray observations of a merged sample of AGN to construct Fig. 2, which shows how $\alpha_{\rm OX}$ changes as a function of Eddington ratio. For AGN at high accretion rates, we use a sample of 150 broad-line AGN from the XMM-COSMOS survey [25], each with spectroscopic $M_{\rm BH}$ estimates, as well as measurements of their $\alpha_{\rm OX}$ and $L_{\rm bol}/L_{\rm Edd}$[26]. For AGN at low accretion rates, we use a sample of six changing-look quasars previously discovered to have undergone dramatic fading in repeat optical spectroscopy[15–17] from the Sloan Digital Sky Survey (SDSS) from a bright state to a current faint state (shown in Fig. 1). The XMM-COSMOS AGN and changing-look quasar samples have narrow $M_{\rm BH}$ distributions that are nearly identical. To determine the $\alpha_{\rm OX}$ of our changing-look quasars after they fade, we obtain *Chandra X-ray Observatory* images to measure the current X-ray luminosities, and we model the faint state SDSS optical spectra to extrapolate the UV luminosities after subtraction of their host galaxy starlight (although our results are not dependent on this extrapolation, see Methods). We verify that each changing-look quasar remains in a faint state during these *Chandra* observations by obtaining an additional, contemporaneous optical spectrum (also shown in Fig. 1). To measure $L_{\rm bol}/L_{\rm Edd}$, we use a bolometric correction to determine the bolometric luminosity of each quasar, and determine $M_{\rm BH}$ based on the prominent broad H Balmer emission lines in its bright state SDSS spectrum. Figure 2 displays not only these measurements of changing-look quasars after their fading to a faint state, but also constraints from their former bright state. To determine the bright state $\alpha_{\rm OX}$, we also model their bright state SDSS spectra to extrapolate UV luminosities. However, only one changing-look quasar (J0159) has an archival X-ray detection[4] close in time to its bright state SDSS spectrum; for the rest we use upper limits on their X-ray luminosities from the *ROSAT* All-Sky Survey, resulting in lower limits on the bright state $\alpha_{\rm OX}$. Although these lower limits on the bright state $\alpha_{\rm OX}$ are weak, their inclusion in Fig. 2 illustrates the decrease in $L_{\rm bol}/L_{\rm Edd}$ of faded changing-look quasars. Additional details on our analysis can be found in Methods.

Our observations reveal that accretion rate changes in AGN correspond to spectral changes that are remarkably similar to those observed in X-ray binaries. Figure 2 directly compares our sample of AGN to the predicted change in $\alpha_{\rm OX}$ for AGN accretion state transitions, scaled from observations of the X-ray binary GRO J1655-40 as it transitioned between the low/hard and high/soft states during a prototypical outburst in 2005[27]. These predictions assume that AGN accretion flows have the same structure as X-ray binaries, and thus directly scale the observed thin disc and coronal components in the X-ray spectra of GRO J1655-40 to supermassive black holes (see Methods for details). The resulting predicted $\alpha_{\rm OX}$ values for AGN in Fig. 2 assume a log-normal distribution of $M_{\rm BH}$ with mean $\langle \log M_{\rm BH} \rangle = 8.4$ and standard deviation $\sigma_{\log M_{\rm BH}} = 0.3$ that matches the XMM-COSMOS AGN and changing-look quasar samples. This direct comparison in Fig. 2 reveals a remarkable similarity between the observed spectral evolution of AGN and X-ray binaries as a function of accretion rate. Specifically, there is a spectral hardening (decreasing $\alpha_{\rm OX}$) in both AGN and X-ray binaries as $L_{\rm bol}/L_{\rm Edd}$ decreases from the high/soft state to the low/hard state, and a spectral softening (increasing $\alpha_{\rm OX}$) below $L_{\rm bol}/L_{\rm Edd} \lesssim 10^{-2}$.

The analogous spectral evolution of X-ray binaries and AGNs implies that the geometry and overall structure of AGN accretion flows are scaled-up versions of those in X-ray binaries, which enables us to use popular models of X-ray binary accretion states to interpret AGN phenomenology. Figure 3 illustrates the application of one such X-ray binary model to describe the evolving geometry of AGN accretion flows during state transitions, based on truncated accretion discs[6]. AGN at Eddington ratios between $10^{-1} \lesssim L_{\rm bol}/L_{\rm Edd} \lesssim 1$ have thin accretion discs with strong thermal UV emission that result in soft $\alpha_{\rm OX}$; these objects represent the AGN equivalent of the high/soft state in X-ray binaries. As the Eddington ratio decreases towards $L_{\rm bol}/L_{\rm Edd} \sim 10^{-2}$, the thin disc becomes progressively truncated as the inner region turns into a radiatively inefficient accretion flow, producing a decrease in UV luminosity and a hardening of $\alpha_{\rm OX}$; this represents the AGN transition to a low/hard state. Below $L_{\rm bol}/L_{\rm Edd} \lesssim 10^{-2}$, the hot inner portion of the disc that produces the optically-thick thermal UV emission is absent, and some other (e.g., synchrotron) emission increasingly dominates the UV, causing $\alpha_{\rm OX}$ to soften again. These AGN are at lower accretion rates in the low/hard state, but above the $L_{\rm bol}/L_{\rm Edd} \lesssim 10^{-5}$ typically associated with the quiescent accretion state in X-ray binaries. In Methods, we also apply an alternative model of X-ray binary accretion state transitions, in which the thin disc is not truncated but rather displays changes in apparent temperature.

An important implication of the analogous nature of black hole accretion flows is that comparative studies can provide new insights into AGN from X-ray binaries, and vice versa. For example, observations of the spectral softening below $L_{\rm bol}/L_{\rm Edd} \lesssim 10^{-2}$ in the low/hard state of X-ray binaries have already suggested that their soft X-ray emission cannot be dominated by optically-thick thermal emission from a truncated thin disc[9], which can only produce spectral hardening. Instead, a new emission component must dominate the soft X-rays in this regime, such as cyclo-synchrotron emission from an advection dominated accretion flow[28] or jet synchrotron emission[29]. Our finding of an analogous softening of $\alpha_{\rm OX}$ in AGN thus suggests that the faint UV/optical continuum in AGN below $L_{\rm bol}/L_{\rm Edd} \lesssim 10^{-2}$ may also be dominated by synchrotron emission. Conversely, inconsistencies in the AGN/X-ray binary analogy can highlight differences in their accretion physics. For example, observations of X-ray binary outbursts show that decreases in accretion rate by factors of $\sim$100 occur on typical timescales of a few days; a simple linear scaling with black hole mass predicts similar behaviour to occur in AGN on timescales of 10^{4-5} years. Yet, we find that changing-look quasars can undergo decreases in accretion rate by factors of $\sim$100 on timescales of $<$10 years, significantly faster than predicted. This discrepancy in variability timescales may thus support recent suggestions of the importance of magnetic pressure in shortening the timescales for changes in accretion discs around supermassive black holes[24,30].

References

1. Shakura, N. I. & Sunyaev, R. A. Black holes in binary systems. Observational appearance. *Astron. Astrophys.* **24**, 337-355 (1973).
2. Shapiro, S. L., Lightman, A. P. & Eardley, D. M. A two-temperature accretion disc model for Cygnus X-1 - Structure and spectrum. *Astrophys. J.* **204**, 187-199 (1976).
3. Remillard, R. A. & McClintock, J. E. X-Ray Properties of Black-Hole Binaries. *Annu. Rev. Astron. Astrophys* **44**, 49-92 (2006).
4. Lamassa, S. M. *et al.* The discovery of the first "changing look" quasar: new insights into the physics and phenomenology of active galactic nucleus. *Astrophys. J.* **800**, 144 (2015).
5. Homan, J. & Belloni, M. The Evolution of Black Hole States. *Ap&SS* **300**, 107-117 (2005).

6. Done, C., Gierliński, M. & Kubota, A. Modelling the behaviour of accretion flows in X-ray binaries. Everything you always wanted to know about accretion but were afraid to ask. *A&A Rev.* **15**, 1-66 (2007).
7. Esin, A. A., McClintock, J. E. & Narayan, R. Advection-Dominated Accretion and the Spectral States of Black Hole X-Ray Binaries: Application to Nova Muscae 1991. *Astrophys. J.* **489**, 865-889 (1997).
8. Narayan, R. & Yi, I. Advection-dominated accretion: A self-similar solution. *Astrophys. J.* **428**, L13-L16 (1973).
9. Sobolewska, M. A., Papadakis, I. E., Done, C. & Malzac, J. Evidence for a change in the X-ray radiation mechanism in the hard state of Galactic black holes. *Mon. Not. R. Astron. Soc.* **417**, 280-288 (2011).
10. Merloni, A., Heinz, S. & di Matteo, T. A Fundamental Plane of black hole activity. *Mon. Not. R. Astron. Soc.* **345**, 1057-1076 (2003).
11. Falcke, H., Körding, E. & Markoff, S. A scheme to unify low-power accreting black holes. Jet-dominated accretion flows and the radio/X-ray correlation. *Mon. Not. R. Astron. Soc.* **414**, 895-903 (2004).
12. Körding, E. G., Jester, S. & Fender, R. Accretion states and radio loudness in active galactic nuclei: analogies with X-ray binaries. *Mon. Not. R. Astron. Soc.* **372**, 1366-1378 (2006).
13. McHardy, I. M. *et al.* Active Galactic Nuclei as scaled-up Galactic black holes. *Nature* **444**, 730-732 (2006).
14. Yang, Q. J. *et al.* Correlation between the photon index and X-ray luminosity of black hole X-ray binaries and active galactic nuclei: observations and interpretation. *Mon. Not. R. Astron. Soc.* **447**, 1692-1704 (2015).
15. Ruan, J. J. *et al.* Toward an understanding of changing-look quasars: an archival search in SDSS. *Astrophys. J.* **826**, 188 (2016).
16. Runnoe, J. C. *et al.* Now you see it, now you don't: the disappearing central engine of the quasar J1011+5442. *Mon. Not. R. Astron. Soc.* **455**, 1691-1701 (2016).
17. MacLeod, C. L. *et al.* A systematic search for changing look quasars in SDSS. *Mon. Not. R. Astron. Soc.* **457**, 389-404 (2016).
18. Yang, Q. *et al.* Discovery of 21 New Changing-look AGNs in the Northern Sky. *Astrophys. J.* **862**, 109 (2018).
19. MacLeod, C. L. *et al.* Changing-Look Quasar Candidates: First Results from Follow-up Spectroscopy. https://arxiv.org/abs/1810.00087 (2018).
20. Fabian, A. C., Vasudevan, R. V. & Gandhi, P. The effect of radiation pressure on dusty absorbing gas around active galactic nuclei. *Mon. Not. R. Astron. Soc.* **385**, L43-L47 (2008).
21. Sheng, Z. *et al.* Mid-infrared Variability of Changing-look AGNs. *Astrophys. J.* **846**, L7 (2017).
22. Stern, D. *et al.* A Mid-IR Selected Changing-look Quasar and Physical Scenarios for Abrupt AGN Fading. *Astrophys. J.* **864**, 27 (2018).
23. Ross, N. P. *et al.* A new physical interpretation of optical and infrared variability in quasars. *Mon. Not. R. Astron. Soc.* **480**, 4468-4479 (2018).
24. Noda, H. & Done, C. Explaining changing-look AGN with state transition triggered by rapid mass accretion rate drop. . *Mon. Not. R. Astron. Soc.* **480**, 3898-3906 (2018).
25. Cappelluti, N. *et al.* The XMM-Newton wide-field survey in the COSMOS field. The point-like X-ray source catalogue. *Astron. Astrophys.* **497**, 635-648 (2009).
26. Lusso, E. *et al.* The X-ray to optical-UV luminosity ratio of X-ray selected type 1 AGN in XMM-COSMOS. *Astron. Astrophys.* **512**, A34 (2010).
27. Sobolewska, M. A., Siemiginowska, A. & Gierliński, M. Simulated spectral states of active galactic nuclei and observational predictions. *Mon. Not. R. Astron. Soc.* **413**, 2259-2268 (2011).
28. Narayan, R. & Yi, I. Advection-dominated Accretion: Underfed Black Holes and Neutron Stars. *Astrophys. J.* **452**, 710 (1995).
29. Markoff, S., Nowak, M. A. & Wilms, J. Going with the Flow: Can the Base of Jets Subsume the Role of Compact Accretion disc Coronae?. *Astrophys. J.* **635**, 1203-1216 (2005).
30. Dexter, J. & Begelman, M. C. Extreme AGN variability: evidence of magnetically elevated accretion?. *Mon. Not. R. Astron. Soc.* **483**, L17-L21 (2019).

Acknowledgements J.J.R. thanks the organizers and participants of the 'Unveiling the Physics Behind Extreme AGN Variability Conference' in 2017 for discussions, and Melania Nynka for guidance on reduction of the *Chandra* X-ray data.

J.J.R., S.F.A., and M.E. are supported by *Chandra* Award Numbers GO7-18101A and GO8-19090A, issued by the *Chandra* X-ray Observatory center, which is operated by the Smithsonian Astrophysical Observatory for and on behalf of the National Aeronautics Space Administration (NASA) under contract NAS8-03060. C.L.M, P.J.G., S.F.A., and J.J.R. are supported by the National Science Foundation under Grants No. AST-1715763 and AST-1715121. J.J.R. and D.H. acknowledge support from a Natural Sciences and Engineering Research Council of Canada (NSERC) Discovery Grant and a Fonds de recherche du Québec-Nature et Technologies (FRQNT) Nouveaux Chercheurs Grant. J.J.R. acknowledges funding from the McGill Trottier Chair in Astrophysics and Cosmology. J.J.R. acknowledges support from the Dan David Foundation. D.H. acknowledges support from the Canadian Institute for Advanced Research (CIFAR).

The scientific results reported in this article are based to a significant degree on observations made by the *Chandra* X-ray Observatory for articles by the PI team, data obtained from the *Chandra* Data Archive for articles based on archival data, observations made by the *Chandra* X-ray Observatory and published previously in cited articles for articles based on published results.

This work used the *ROSAT* Data Archive of the Max-Planck-Institut für extraterrestrische Physik (MPE) at Garching, Germany.

This work used observations obtained with *XMM-Newton*, an ESA science mission with instruments and contributions directly funded by ESA Member States and NASA.

This work used observations obtained with the Apache Point Observatory 3.5-meter telescope, which is owned and operated by the Astrophysical Research Consortium.

Funding for the Sloan Digital Sky Survey IV has been provided by the Alfred P. Sloan Foundation, the U.S. Department of Energy Office of Science, and the Participating Institutions. SDSS-IV acknowledges support and resources from the center for High-Performance Computing at the University of Utah. The SDSS web site is www.sdss.org.

SDSS-IV is managed by the Astrophysical Research Consortium for the Participating Institutions of the SDSS Collaboration including the Brazilian Participation Group, the Carnegie Institution for Science, Carnegie Mellon University, the Chilean Participation Group, the French Participation Group, Harvard-Smithsonian center for Astrophysics, Instituto de Astrofísica de Canarias, The Johns Hopkins University, Kavli Institute for the Physics and Mathematics of the Universe (IPMU) / University of Tokyo, the Korean Participation Group, Lawrence Berkeley National Laboratory, Leibniz Institut für Astrophysik Potsdam (AIP), Max-Planck-Institut für Astronomie (MPIA Heidelberg), Max-Planck-Institut für Astrophysik (MPA Garching), Max-Planck-Institut für Extraterrestrische Physik (MPE), National Astronomical Observatories of China, New Mexico State University, New York University, University of Notre Dame, Observatário Nacional / MCTI, The Ohio State University, Pennsylvania State University, Shanghai Astronomical Observatory, United Kingdom Participation Group, Universidad Nacional Autónoma de México, University of Arizona, University of colourado Boulder, University of Oxford, University of Portsmouth, University of Utah, University of Virginia, University of Washington, University of Wisconsin, Vanderbilt University, and Yale University.

Author contributions J.J.R. led the data collection, analysis, and interpretation, as well as the manuscript preparation. J.J.R. and S.F.A. obtained the ARC 3.5m spectra. J.J.R., S.F.A., M.E., P.J.G., C.L.M., and J.C.R. proposed for the *Chandra* X-ray observations. M.A.S. provided the results from modeling of X-ray binary outbursts. All authors discussed the interpretation of the results.

Additional information **Supplementary information** is available for this paper.

Correspondence and requests for materials should be addressed to J.J.R. (email: john.ruan@mcgill.ca).

Competing Interests The authors declare that they have no competing financial interests.

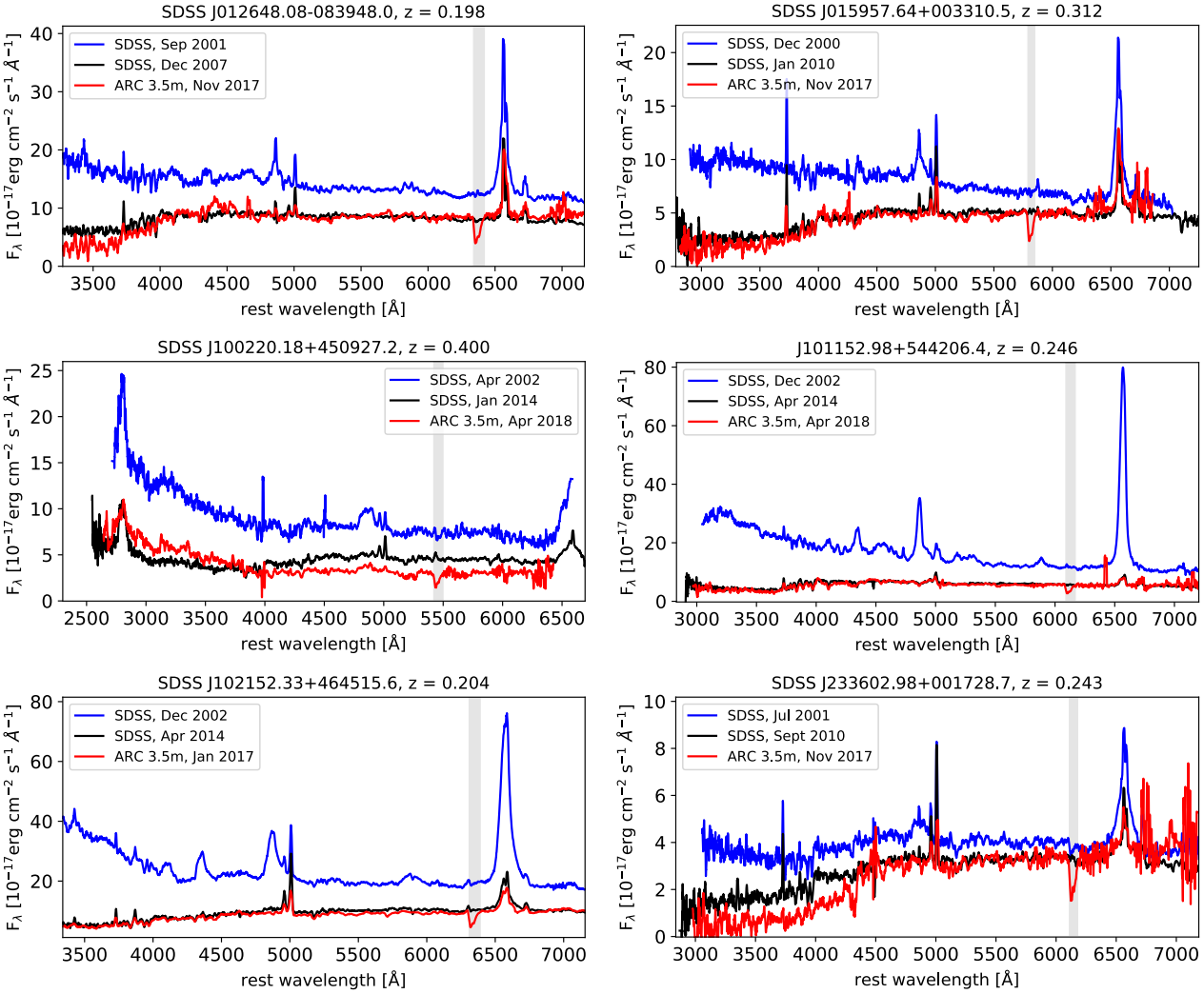

Figure 1: **Multi-epoch optical spectroscopy reveals the dramatic fading of changing-look quasars.** Repeat SDSS spectra of six changing-look quasars over ∼10 years shows a fading of the broad emission lines and continuum from a bright state (blue) to a faint state (black), consistent with a decrease in their accretion rates. A more recent epoch of spectra from the ARC 3.5m telescope is also shown (red), which verifies that these changing-look quasars are still in a faint state contemporaneous with our *Chandra* X-ray observations. Wavelength regions affected by telluric absorption are shaded grey.

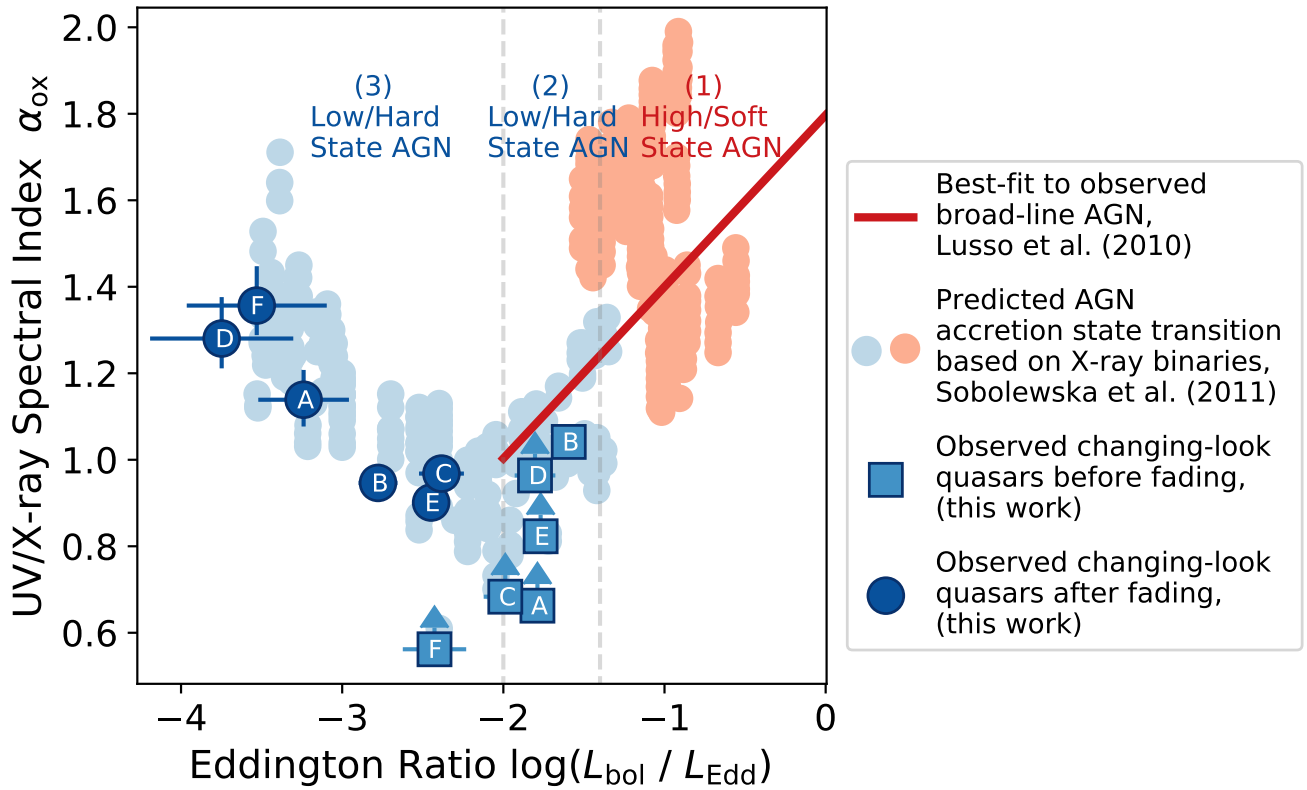

Figure 2: **The spectral behaviour of AGN and X-ray binaries are remarkably similar across a wide range of Eddington ratios.** The UV-to-X-ray spectral index ($\alpha_{\rm OX}$) of changing-look quasars before their fading (light blue squares) and after their fading (dark blue circles) are shown, as well as the fit to a large sample of more luminous broad-line AGN from the XMM-COSMOS survey (red line). These observations are directly compared to predictions for accretion state transitions in AGN, based on observations of X-ray binary transitions from a high/soft state (light red circles) to a low/hard state (light blue circles). The remarkable similarity in the spectral behaviour of AGN and X-ray binaries suggests that the geometries of black hole accretion flows are analogous. The lettered labels correspond to different changing-look quasars in our sample: (A) J0126, (B) J1059, (C) J1002, (D) J1011, (E) J1021, and (F) J2336. A model for the geometry of the disc-corona system that corresponds to the labeled ranges in $L_{\rm bol}/L_{\rm Edd}$ is presented in Fig. 3.

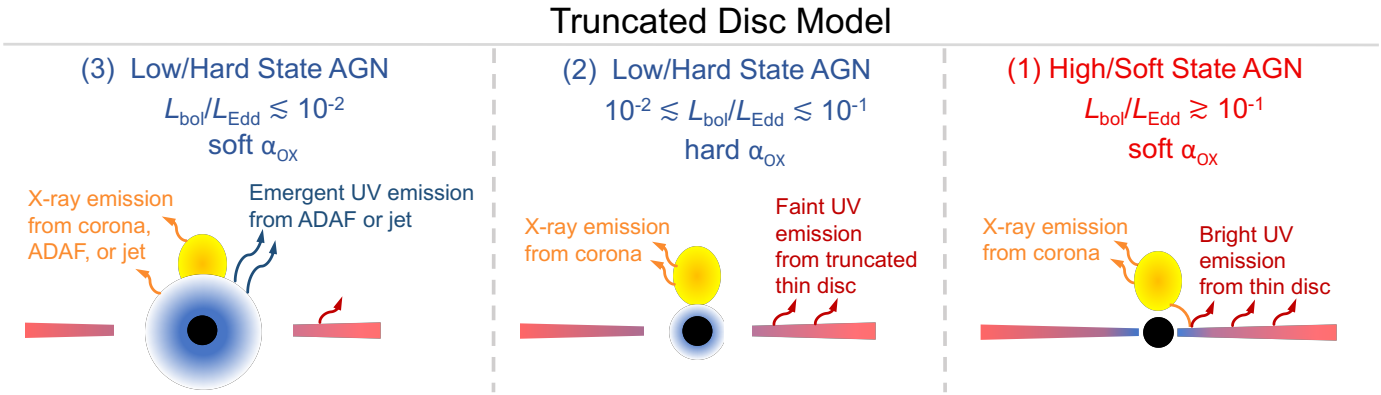

Figure 3: **A model for the geometry of AGN accretion flows in different accretion states.** The analogous geometries of black hole accretion flows enables us to use popular models of X-ray binary accretion states to interpret AGN phenomenology. The panels illustrate the application of one such X-ray binary model based on truncated discs to describe the accretion flow in fading AGN, over ranges of Eddington ratio that correspond to those labeled in Fig. 2. Right panel: At high accretion rates ($L_{\rm bol}/L_{\rm Edd} \gtrsim 10^{-1}$) in the high/soft state, the soft $\alpha_{\rm OX}$ is due to bright UV emission from a thin accretion disc. Centre panel: As the accretion rate drops ($10^{-2} \lesssim L_{\rm bol}/L_{\rm Edd} \lesssim 10^{-1}$), the inner regions of the thin disc become progressively truncated and the AGN enters the low/hard state. The truncation of the inner disc causes the UV luminosity to fade, and thus $\alpha_{\rm OX}$ hardens. Left panel: At low accretion rates ($L_{\rm bol}/L_{\rm Edd} \lesssim 10^{-2}$), the $\alpha_{\rm OX}$ softens again due to the emergence of UV emission from either an advection dominated accretion flow or a jet. An alternative model without disc truncation is presented in Methods.

Methods

Faint state X-ray fluxes from *Chandra*

To measure the X-ray fluxes of our changing-look quasars after they have faded to a faint state, we obtain new *Chandra* X-ray observations. The details of these observations are listed in Supplementary Table 3, and their derived faint state luminosities ($\nu L_{2\rm keV}$) that are used to calculate $\alpha_{\rm OX}$ values are listed in Supplementary Table 5. Throughout this work, we assume a standard ΛCDM cosmology with $\Omega_{\rm m} = 0.309$, $\Omega_\Lambda = 0.691$, and $H_0 = 67.7$ km s^{-1} Mpc^{-1}[31].

For five of our sample of six changing-look quasars, we obtain new *Chandra* X-ray observations through a *Chandra* Cycle 18 Guest Observer program (PI: Ruan, Program Number: 18700505). For the one other changing-look quasar in our sample (J0159), we use similar *Chandra* observations that were obtained in a separate Cycle 17 GTO program (PI: Predehl, Program Number: 17700782). All observations are obtained using the ACIS-S3 chip in VFAINT mode, and their exposure times are listed in Supplementary Table 3. We use the CIAO v.4.9 (CALDB v4.7.7) software[32] for reduction and analysis of the resultant X-ray data.

We reprocess the level 2 events files and use CIAO's *repro* script to apply the latest calibrations. We then generate both a 0.5 - 7 keV X-ray counts image and a PSF image of the ACIS-S3 chip. To perform source detection and obtain X-ray positions, we use the *wavedetect* script. All of our six sources are detected in the *Chandra* observations, and all of their measured X-ray positions are each within $0\farcs6$ of their optical positions from SDSS imaging. Since X-ray emission from our changing-look quasars is expected to be point-like, we use the *srcflux* tool to extract source counts at the X-ray position of each object. The source extraction region radii are set to encompass 90% of the PSF at 1 keV, and the PSF contributions in the source and background regions are estimated using the *arfcorr* tool. The resultant 0.5 - 7 keV source count rates for the changing-look quasars are listed in Supplementary Table 3.

For five of our six objects, the source counts are insufficient to extract a high-quality X-ray spectrum, and thus we assume a fixed spectral model to compute fluxes. Specifically, we assume a power-law spectral model with $\Gamma = 1.8$, typical for low-luminosity AGN[33–35]. We test the effects of adopting a range in Γ from 1.6 to 2.0, and find that this produced systematic uncertainties on the resulting X-ray fluxes of $\lesssim$5% (and $\ll$1% on the resulting $\alpha_{\rm OX}$). Thus, the uncertainties on our X-ray fluxes are dominated by measurement uncertainties, and we ignore the negligible systematics that stem from our assumptions for Γ. In our spectral model, we include Galactic absorption based on neutral hydrogen column densities[36]. For one object (J1002), the source counts are sufficient for us to extract and fit its X-ray spectrum. We use Sherpa to fit a power-law spectral model with Galactic absorption, using atomic cross sections[37] and abundances[38]. The best-fitting spectral model has $\Gamma = 1.8 \pm 0.1$, and we compute the X-ray flux for J1002 from this fit. The resultant 0.5 - 7 keV unabsorbed model fluxes for our all changing-look quasars are listed in Supplementary Table 3. Finally, we calculated X-ray luminosities at rest-frame 2 keV using the WebPIMMs tool, and these $\nu L_{2\rm keV}$ measurements are listed in Supplementary Table 5.

ARC 3.5m optical spectra

To verify that our changing-look quasars are still in a faint state during the *Chandra* observations and have not re-brightened in the optical, we obtain a more recent epoch of optical spectroscopy within a few months of each *Chandra* observation. Details of these follow-up observations are listed in Supplementary Table 2.

We use the Dual Imaging Spectrograph on the Astrophysical Research Consortium (ARC) 3.5m telescope at Apache Point Observatory to obtain a long-slit optical spectrum for each changing-look quasar. For each spectrum, we use the B400/R300 grating (spectral resolution of R $\sim$ 1000 and wavelength coverage of $\lambda \sim$ 3400 - 9200 Å), with a $1\farcs5$ slit. The total exposure times range from 45 to 90 min, and the observations are taken at mean airmasses between 1.03 to 1.35, with seeing between $1\farcs2$ to $1\farcs6$. Additional spectra of spectrophotometric standard stars are obtained on each night for flux-calibration, and HeNeAr lamps are used for wavelength calibration. We reduce these optical spectra using standard IRAF[39] procedures, including bias and flat-field correction, wavelength- and flux-calibration, and corrections for atmospheric extinction. Finally, we correct for Galactic extinction using the dust maps[40] and a Milky Way reddening law[41].

The reduced APO spectra are shown in Fig. 1, and show that the broad emission lines and continuum emission remain faint for all of our changing-look quasars. This demonstrates that our changing look quasars are all still in a faint state contemporaneous with the *Chandra* observations, and did not re-brighten back to a bright state. However, we opt to use the bright and faint state SDSS spectra in all our analysis (e.g. to measure $\alpha_{\rm OX}$) rather than these APO spectra, due to the superior spectrophotometric calibration of SDSS spectroscopy.

Bright state X-ray fluxes from *ROSAT* and *XMM-Newton*

We use archival X-ray observations to constrain the rest-frame unabsorbed 2 keV luminosities $\nu L_{2\rm keV}$ for our sample of changing-look quasars in their former bright state. Although only one changing-look quasar in our sample actually has an archival bright state X-ray detection (from *XMM-Newton*), we derive upper limits on $\nu L_{2\rm keV}$ from *ROSAT* for the remainder of our sample so these bright state datapoints can be included in Fig. 2, thus showing their change in $L_{\rm bol}/L_{\rm Edd}$ as they fade. The list of bright state X-ray observations we use in our analysis is provided Supplementary Table 4, and the derived bright state $\nu L_{2\rm keV}$ values are listed in Supplementary Table 5.

We first search the ESA *XMM-Newton* Upper Limit Server[a] and find that a deep pointed *XMM-Newton* observation was obtained for J0159 from 7 July 2000, close in time to its bright state SDSS spectrum from 23 Dec 2000. Previously, the X-ray spectrum from this *XMM-Newton* observation was reduced and fitted to derive a 2 - 10 keV flux[4]. We use the WebPIMMs tool to convert this 2 - 10 keV flux to a $\nu L_{2\rm keV}$, assuming the best-fit power-law spectral model (with $\Gamma = 2.13$ and no intrinsic absorption), and accounting for Galactic absorption. For the remaining five changing-look quasars in our sample, two (J1002 and J1021) were observed as part of the *XMM-Newton* Slew Survey, but were not detected. We chose not to use these upper limits from *XMM-Newton* Slew Survey observations for J1002 and J1021 in our analysis, because these observations were obtained in the period between the bright and faint state SDSS spectra. Thus, J1002 and J1021 were in the middle of their observed fading at the time of the *XMM-Newton* Slew Survey observations. Furthermore, the short exposures (<10 sec) in these *XMM-Newton* Slew Survey observations do not provide useful upper limits on the X-ray fluxes (and are worse than upper limits from *ROSAT* observations).

For the five changing-look quasars in our sample without *XMM-Newton* detections, we use archival *ROSAT* X-ray data to provide constraints on the bright state X-ray flux. None of these objects were detected in any *ROSAT* catalogs from pointed or scan observations, and so we use processed *ROSAT* All-Sky Survey images from the MPE *ROSAT* Data Archive[b] to derive upper limits. For each image, we use the SOSTA tool in the XIMAGE[c] software package to calculate 3σ upper limits at the position of each changing-look quasar, which accounts for variations in the background level, effects of vignetting, and effec-

[a] http://xmm.esac.esa.int/UpperLimitsServer/
[b] http://www.xray.mpe.mpg.de/cgi-bin/rosat/rosat-survey
[c] https://heasarc.gsfc.nasa.gov/docs/xanadu/ximage/ximage.html

tive exposure time in the images. Our 0.1 - 2.4 keV upper limits on the *ROSAT* count rates of these five changing look quasars are in the range of 0.11 - 0.42 cts s^{-1}, consistent with the overall estimated upper limit of 0.1 cts s^{-1} for undetected sources in the *ROSAT* All-Sky Survey[42]. We convert these count rates to $\nu L_{2\rm keV}$ using WebPIMMs[d], also assuming a power-law spectral model with $\Gamma = 1.8$ and accounting for Galactic absorption. These *ROSAT* upper limits on the bright state X-ray fluxes are also listed in Supplementary Table 4.

We emphasize that these upper limits on the bright state X-ray fluxes from *ROSAT* do not provide strong constraints on the bright state $\alpha_{\rm OX}$ (shown as lower limits in Fig. 2). This is primarily because the *ROSAT* observations were obtained $\sim$10 years before the bright state SDSS spectra, and thus it is unclear if the changing-look quasars were in a bright or faint state during the *ROSAT* observations. Nevertheless, we display these bright state upper limits in Fig. 2 to illustrate the change in $L_{\rm bol}/L_{\rm Edd}$ of each changing-look quasar, which demonstrates that they are already in a low/hard accretion state even before their fading.

Decomposition of SDSS optical spectra and host galaxy subtraction

All of the analysis of our Sloan Digital Sky Survey (SDSS)[43] optical spectra is performed on the decomposed quasar spectra, which are the observed SDSS optical spectra after the host galaxy components have been subtracted. To perform this host galaxy subtraction, we decompose each spectrum into quasar and host galaxy components by fitting a mixture of quasar and galaxy eigenspectra[15,44,45], created from principal component analysis (PCA) of large samples of SDSS spectra[46,47]. After subtracting the best-fit host galaxy component from the observed spectrum, we use the resultant decomposed quasar spectrum and the reported measurement uncertainties in the SDSS spectrum in our spectral modelling. For each of our changing-look quasars, we perform this decomposition process for both its bright and faint state SDSS spectrum.

We note that for one changing-look quasar in our sample (J2336), there are four bright state SDSS spectra available, all obtained within a period of approximately two years (MJDs of 51783, 51877, 52199, 52525). Since there is no significant variation among these four bright state spectra of J2336, we co-add them into one mean bright state spectrum to use in our spectral analysis of this object. For the MJD of this mean bright state spectrum of J2336, we simply adopt the mean MJD from the four spectra of 52096.

We first correct our SDSS spectra for Galactic extinction, also using dust maps[40] and a Milky Way reddening law[41]. To enable fitting of the eigenspectra, we then resample all the SDSS spectra and eigenspectra onto a common rest-frame wavelength grid of the form $\log(\lambda) = 3.35 + 0.0001a$, for integer a from 0 to 5900. This common wavelength grid is chosen to accommodate the rest-frame wavelength range of all our spectra, and is similar to the native SDSS spectral resolution. We next use the first five galaxy eigenspectra[47], and the first five quasar eigenspectra (excluding the second quasar eigenspectrum, which primarily describes the host galaxy)[46], which captures >98% of the variance in SDSS quasar and galaxy spectra. We then perform a simple χ^2 fit of this mixture of eigenspectra to each SDSS spectrum, with 10 total eigenspectra amplitudes (i.e., PCA coefficients) as free parameters. In our tests, increasing the number of eigenspectra components used in our decomposition to 10 quasar eigenspectra and 10 galaxy eigenspectra does not significantly improve our fits. Furthermore, we verify that using Markov Chain Monte Carlo algorithms to perform this decomposition results in the same fitting results as our simple χ^2 method. However, we chose to use the computationally faster χ^2 fit to enable Monte Carlo resampling of the observed spectra to robustly estimate uncertainties on all derived optical spectral properties.

The best-fit quasar and galaxy components for both the bright and faint state SDSS spectrum from our decomposition of each changing-look quasar are shown in Supplementary Figs. 1-6. The decomposed quasar spectra (i.e., after the host galaxy component is subtracted) are also shown in Supplementary Figs. 1-6. We next fit these decomposed quasar spectra to derive various optical properties.

Broad emission line fitting in SDSS spectra

To estimate the Eddington luminosity $L_{\rm Edd}$ for each changing-look quasar, we first fit the prominent broad H Balmer emission lines in their bright state decomposed quasar spectra to obtain viral black holes masses ($M_{\rm BH}$). Whenever possible, we chose to fit the broad Hα line in the bright state decomposed quasar spectra, due to its higher signal-to-noise ratio in our spectra in comparison to other less-prominent broad emission lines. Our spectral model for Hα includes a power-law continuum component that we fit to the continuum wavelength windows of [6400, 6500] Å and [6800, 7000] Å surrounding the Hα line. In the Hα line wavelength window of [6500, 6800] Å, we included Gaussian emission line components for broad Hα, narrow Hα, the narrow [N II] $\lambda\lambda$6548, 6584 doublet, and the narrow [S II] $\lambda\lambda$6717, 6731 doublet. In our fitting, we constrain the redshifts of the narrow emission lines to be the same, and their widths to be <1200 km s^{-1}. Furthermore, we constrain the width of the broad Hα emission to be >1200 km s^{-1}, while its central wavelength is left as a free parameter.

For one quasar (J1002), Hα is redshifted out of the wavelength range of the eigenspectra, and thus we instead fit the Hβ line in its bright state decomposed quasar spectrum. The Hβ spectral model for J1002 includes a power-law continuum and an optical Fe II template[49] that we fit in the continuum wavelength windows of [4435, 4700] Å and [5100, 5535] Å surrounding the Hβ line. In the Hβ line wavelength window of [4700, 5007] Å, we include Gaussian emission line components for broad Hβ, narrow Hβ, and the narrow [O III] $\lambda\lambda$4959,5007 doublet. Similar to our fitting procedure for Hα, we constrain the redshifts of the narrow lines to be the same, and their widths to be <1200 km s^{-1}, while we constrain the width of broad Hβ to be >1200 km s^{-1}, and its central wavelength is left as a free parameter.

We fit our broad Hα and Hβ line models to the decomposed quasar spectrum of each changing-look quasar using a simple χ^2 fit. The best-fit models to the spectra are also shown in Supplementary Figs. 1-6. The Full-Width at Half-Maximum (FWHM) of the broad emission components in the bright state spectra are listed in Supplementary Table 1; these FWHM values are later combined with the 5100 Å continuum luminosities ($\lambda L_{5100\rm \AA}$) to estimate $M_{\rm BH}$ for each changing-look quasar.

Continuum fitting in SDSS spectra

We separately fit the continuum emission in both the bright and faint state SDSS spectrum of each changing-look quasar. We fit the continuum emission over the rest-frame [3500, 6000] Å wavelength range, avoiding wavelength windows that contain prominent emission lines. Specifically, we exclude the following wavelength regions in our continuum fit: [3714, 3740] Å for [O II] λ3728; [3850, 3884] Å for [Ne III] λ3869; [4050, 4152] Å for Hδ λ4103; [4285, 4412] Å for Hγ λ4342; [4352, 4372] Å for [O III] λ4364; [4760, 4980] Å for Hβ λ4863; [4945, 4972] Å for [O III]λ 4960; [4982, 5035] Å for [O III] λ5008; and [5805, 5956] Å for He I λ5877. The wavelength ranges for these prominent emission lines are based on the composite SDSS quasar spectrum[48].

Our continuum model components include a power-law, a template for optical Fe II emission[49], a model for blended high-order H Balmer broad emission lines, and a model for the Balmer continuum. At wavelengths blueward of the Blamer limit (3546 Å), the Balmer

[d] http://cxc.harvard.edu/toolkit/pimms.jsp

continuum can produce a significant contribution to the observed continuum emission. We thus generate model spectra for the Balmer continuum, based on a parameterized form[50,51]. In this model, the Balmer continuum is an absorbed Planck function at electron temperature $T_{\rm e}$. This function vanishes redward of the Balmer limit, and has the form $f = B(T_{\rm e})(1 - e^{-\tau_\nu})$ blueward of the Balmer limit, where τ_ν is the optical depth $\tau_\nu = \tau_0(\lambda/\lambda_B)^3$. We fixed $T_{\rm e}$ to 15,000 K since variations in $T_{\rm e}$ within the range of 8,000 - 20,000 K have a negligible effect on the resulting spectrum in our wavelength range of interest redward of 2000 Å. However, variations in τ_0 will change the slope of resultant Balmer continuum, and thus we compute model Balmer continuum over a grid of varying τ_0 from 0.1 - 2.0, and smooth the resulting spectra with a Gaussian filter of FWHM = 4,000 km s^{-1} to account for broadening due to bulk motions of the gas.

At wavelengths redward of the Balmer limit, high-order H Balmer emission lines blend together to produce a pseudo-continuum that should be included in our spectral fits. We thus generate model spectra for Balmer lines higher than Hϵ with upper levels up to 50, in which each line is represented by a Gaussian using their listed strengths[52]. In these model spectra, we assume Case B recombination, electron temperatures of 15,000 K, and electron number density of 10^{11} cm^{-3}. For each spectrum, we smooth the width of these high-order Balmer emission lines to match the FWHM of the observed broad Hβ emission line.

We fit our continuum model to the decomposed quasar spectra in the continuum windows, using χ^2 minimization. To take into account the τ_0 free parameter in the Balmer continuum spectral model, we perform our fit iteratively, in which we first fit the spectrum assuming an initial fixed τ_0, and then re-fit the spectra leaving τ_0 as a free parameter. The best-fitting τ_0 is then fixed, and this process is repeated until τ_0 converges. We use the best-fit power-law continuum from these fits for our $M_{\rm BH}$ estimates, and extrapolate this power-law continuum for our calculations of $\alpha_{\rm OX}$.

Spectral index $\alpha_{\rm OX}$ measurements

For each changing-look quasar, we calculate both a bright and faint state $\alpha_{\rm OX}$[53], which is the spectral index between the rest-frame 2500 Å luminosity $\lambda L_{2500\mathring{\rm A}}$, and the 2 keV luminosity $\nu L_{\rm 2keV}$. The definition of $\alpha_{\rm OX}$ is thus:

$$\alpha_{\rm OX} = -\frac{\log(\lambda L_{2500\mathring{\rm A}}) - \log(\nu L_{\rm 2keV})}{\log(\nu_{2500\mathring{\rm A}}) - \log(\nu_{\rm 2keV})} + 1. \quad (1)$$

Although the observed optical continua in our SDSS spectra probe the thin accretion disc, they do not span blueward of rest-frame 3500 Å, and thus $\lambda L_{2500\mathring{\rm A}}$ is not directly observed. Since $\lambda L_{2500\mathring{\rm A}}$ is used in the standard definition of $\alpha_{\rm OX}$, we extrapolate the best-fit power-law continuum in each spectrum from our continuum fitting to estimate $\lambda L_{2500\mathring{\rm A}}$. Furthermore, since the predicted spectral behaviour of AGN accretion state transitions that we compare our observations to also uses $\lambda L_{2500\mathring{\rm A}}$ in the definition of $\alpha_{\rm OX}$, this extrapolation of our spectra to 2500 Å enables a direct comparison to X-ray binaries. The resulting bright and faint state $\lambda L_{2500\mathring{\rm A}}$ and $\alpha_{\rm OX}$ values for each changing look quasar in our sample are listed in Supplementary Table 5.

We demonstrate that our results are not strongly dependent on the extrapolation of the power-law continuum in the SDSS spectrum to 2500 Å. Since the observed 3500 Å luminosity covered by our spectra also probes the thin accretion disc emission, we instead calculate $\alpha_{\rm OX}$ using the 3500 Å luminosity (i.e., without extrapolating to 2500 Å). Supplementary Figure 7 shows the behaviour of this alternate $\alpha_{\rm OX}$ as a function of accretion rate, similar to Fig. 2. The clear softening of $\alpha_{\rm OX}$ as the Eddington ratio drops below $L_{\rm bol}/L_{\rm Edd} \lesssim 0.01$ is still observed, and is still an excellent match to predictions from X-ray binary accretion state transitions. This consistency of our results even when using the observed 3500 Å luminosity is largely because our extrapolation of the observed power-law continuum redward of 3500 Å to estmate $\lambda L_{2500\mathring{\rm A}}$ is relatively minor, and only extends the fit over an additional 1000 Å. Furthermore, because $\alpha_{\rm OX}$ is a spectral index that spans $\sim 10^{2.8}$ Hz in frequency, small changes in the optical or X-ray luminosities do not significantly affect $\alpha_{\rm OX}$ (a factor of 2 change in the X-ray or UV flux will change $\alpha_{\rm OX}$ by only 0.11). This explicitly shows that our conclusions are not strongly affected by our extrapolation of the power-law spectral continuum.

Black hole mass estimates

To estimate the $M_{\rm BH}$ for each of our changing-look quasars, we use standard single-epoch spectroscopic $M_{\rm BH}$ estimation methods. In this approach, the single-epoch virial $M_{\rm BH}$ is based on the measured FWHM of a broad H Balmer line, as well as a radius-luminosity relation for the broad-line region from reverberation mapping of low-redshift AGNs. For the five changing-look quasars in our sample for which we measured the FWHM of the prominent broad Hα emission from our spectral fitting, we use the relation[54]:

$$M_{\rm BH,H\alpha} = (9.7 \pm 0.05) \times 10^6 \left[\frac{\rm FWHM(H\alpha)}{1000 \text{ km s}^{-1}}\right]^{2.06\pm0.06} \times \left[\frac{\lambda L_{5100\mathring{\rm A}}}{10^{44} \text{ erg s}^{-1}}\right]^{0.519\pm0.07} M_\odot, \quad (2)$$

which is based on a radius-luminosity relation from reverberation mapping[55]. Similarly, for the Hβ emission line in J1002, we use the relation[56]:

$$M_{\rm BH,H\beta} = 10^{6.91\pm0.02} \left[\frac{\rm FWHM(H\beta)}{1000 \text{ km s}^{-1}}\right]^{2} \times \left[\frac{\lambda L_{5100\mathring{\rm A}}}{10^{44} \text{ erg s}^{-1}}\right]^{0.5} M_\odot. \quad (3)$$

For each of our quasars, we calculate the Eddington ratio using $L_{\rm bol}/L_{\rm Edd} = L_{\rm bol}/(1.3 \times 10^{38}\ M_{\rm BH})$, for $M_{\rm BH}$ in units of $M_\odot$, and $L_{\rm bol}$ in units of erg s^{-1}. The uncertainties on the $M_{\rm BH}$ estimates include the measurement uncertainties on both $\lambda L_{5100\mathring{\rm A}}$ and broad line FWHM, as well as the uncertainties in the single-epoch virial $M_{\rm BH}$ relations (Equations 2 and 3), but do not account for any additional systematics.

Bolometric corrections

To calculate the bolometric Eddington ratio $L_{\rm bol}/L_{\rm Edd}$ for each quasar, we apply an empirical bolometric correction to our observed optical and/or X-ray luminosities to estimate $L_{\rm bol}$. For our faint state observations, we use the bolometric correction[57]:

$$\log(L_{\rm bol}) = \log(\nu L_{\rm 2keV}) + 1.561 - 1.863\alpha_{\rm OX} + 1.266\alpha_{\rm OX}^2. \quad (4)$$

This bolometric correction is dependent on $\alpha_{\rm OX}$, and thus takes into account the change in the spectral energy distribution (SED) shape for AGN at different $L_{\rm bol}/L_{\rm Edd}$. For our bright state observations, only upper limits on the bright state $\nu L_{\rm 2keV}$ (and thus lower limits on $\alpha_{\rm OX}$) are available for the majority of our changing-look quasars. We thus instead use a bolometric correction based on the 3000 Å continuum luminosity[58] ($\lambda L_{3000\mathring{\rm A}}$) for our bright state observations:

$$\log(L_{\rm bol}) = (0.975 \pm 0.028)\log(\lambda L_{3000\mathring{\rm A}}) + (1.862 \pm 1.275). \quad (5)$$

This bolometric correction is based on the SEDs of a sample of broad-line AGN, similar to the bright states of our changing-look quasars. The $\lambda L_{3000\text{Å}}$ measurements are obtained from our power-law continuum fits to the SDSS spectra. We note that for J0159 (the one changing-look quasar in our sample that has a bright state X-ray detection from *XMM-Newton*), the bright state $L_{\rm bol}$ calculated using Equations 4 and 5 are in good agreement.

Our use of bolometric corrections has caveats that should be considered and tested. The first issue is that the faint state bolometric corrections we use are created using a sample of AGN accreting at $L_{\rm bol}/L_{\rm Edd} > 0.01$, while our changing-look quasars are at lower $L_{\rm bol}/L_{\rm Edd}$ in their faint state. Since we observe an increase in $\alpha_{\rm OX}$ at $L_{\rm bol}/L_{\rm Edd} \lesssim 0.01$ (e.g., in Fig. 2), applying this bolometric correction essentially assumes that the SEDs of AGN at low $L_{\rm bol}/L_{\rm Edd}$ are similar in shape to those at high $L_{\rm bol}/L_{\rm Edd}$ if their $\alpha_{\rm OX}$ are similar. However, this assumption is unlikely to significantly affect our results, since previous calculations of bolometric corrections that probe accretion rates down to $L_{\rm bol}/L_{\rm Edd} \lesssim 0.01$ do indeed show hints of a inflection in the X-ray bolometric correction at $L_{\rm bol}/L_{\rm Edd} \sim 0.01$[59,60]. The second issue is that the bright state bolometric corrections we use are based solely on $\lambda L_{3000\text{Å}}$, and thus do not account for changes in SED shape as a function of $L_{\rm bol}/L_{\rm Edd}$. However, since the bulk of the multi-wavelength emission for luminous AGN is emitted in the UV, and the bright state bolometric correction we used is based on $\lambda L_{3000\text{Å}}$, changes in the X-ray emission as a function of $L_{\rm bol}/L_{\rm Edd}$ will not strongly affect this bolometric correction in this regime.

Although we argue that the bolometric corrections we use in our analysis are unlikely to affect our results, we nevertheless explicitly demonstrate that our conclusions are not strongly dependent on the bolometric corrections. In Supplementary Fig. 8, we show the $\alpha_{\rm OX}$ behaviour of our changing-look quasars as a function of the UV Eddington ratio $\lambda L_{2500\text{Å}}/L_{\rm Edd}$ (i.e. without making any bolometric corrections), in comparison to predictions for accretion state transitions for a 10^8 $M_\odot$ AGN[27]. The softening in $\alpha_{\rm OX}$ below a critical Eddington ratio is still clearly observed, and the changes in $\alpha_{\rm OX}$ remain in good agreement with predictions based on accretion state transitions in X-ray binaries.

Uncertainties on the optical spectral properties

We estimate the uncertainties on all quantities derived from the SDSS optical spectra (e.g., $\lambda L_{2500\text{Å}}$, $M_{\rm BH}$, $L_{\rm bol}/L_{\rm Edd}$, $\alpha_{\rm OX}$, etc.) through Monte Carlo resampling of the observed spectra. We first generate 1000 Monte Carlo realizations of each observed spectrum, based on the reported measurement uncertainties in each wavelength bin. For each resampled spectrum, we then repeat our spectral decomposition for host-galaxy subtraction, broad emission line fitting, and continuum fitting. The 1σ uncertainties on the derived optical spectral quantities are thus the 1σ spread in the 1000 resampled spectral fits.

Comparisons to simulated AGN state transitions

We compare the observed behaviour in $\alpha_{\rm OX}$ for our sample of AGN (including fading changing-look quasars) to predictions for AGN accretion state transitions[27], e.g. in Figs. 2, 7, and 8. These predictions are based on the observed X-ray spectral behaviour of the X-ray binary GRO J1655-40 during accretion state transitions, scaled up to AGN. This X-ray binary hosts a 6.3 $M_\odot$ black hole[3], and underwent a prototypical outburst in 2005 from a low/hard state to a high/soft state, before fading back to a low/hard state. Based on X-ray spectroscopic monitoring of this outburst using the *Rossi X-ray Timing Explorer* (RXTE), previous studies[27] fitted spectral models that include soft X-ray accretion disc[61] and hard X-ray coronal components[62,63], to characterize how its X-ray spectrum changes during the outburst. To scale the observed spectral behaviour of the thin disc component to AGN, these previous studies[27] assumed that the luminosity scales as $L \propto M_{\rm BH}$, while the temperature of the disc component follows the $T \propto M_{\rm BH}^{-1/4}$ scaling for Shakura-Sunyaev discs[1]. For the corona spectral component, it is assumed that the heating-to-cooling compactness ratio of the disc-corona system[64] changes with $L_{\rm bol}/L_{\rm Edd}$ similarly in AGN as observed in GRO J1655-40[27]. The resulting predicted spectral behaviour of accretion state transitions in AGN is then quantified by $\alpha_{\rm OX}$, to enable direct comparisons to observations of AGN.

A direct comparison of the predicted behaviour of $\alpha_{\rm OX}$ to observations of a sample of AGN requires the adoption of a $M_{\rm BH}$ distribution. This is because if there is a spread in the $M_{\rm BH}$ distribution of the AGN sample, the $T \propto M_{\rm BH}^{-1/4}$ scaling of the thin disc temperature at a fixed $L_{\rm bol}/L_{\rm Edd}$ will create an intrinsic spread in $\alpha_{\rm OX}$. To minimize this effect and ensure a fair comparison to X-ray binaries, the AGN sample should have a narrow range in $M_{\rm BH}$, and the predicted $\alpha_{\rm OX}$ from X-ray binaries should match this $M_{\rm BH}$ distribution. The predictions generated[27] in Fig. 2 specifically assume the narrow log-normal $M_{\rm BH}$ distribution from the XMM-COSMOS[25] broad-line AGN[26] (also shown in Fig. 2), with mean $\langle \log M_{\rm BH} \rangle$ = 8.4 and standard deviation of $\sigma_{\log M_{\rm BH}} = 0.3$. Furthermore, this is nearly identical to the $M_{\rm BH}$ distribution our changing-look quasars (see Supplementary Table 1), with $\langle \log M_{\rm BH} \rangle$ = 8.3 and $\sigma_{\log M_{\rm BH}} = 0.2$. Thus, our comparison of a sample of AGN (including changing-look quasars) to predictions from X-ray binaries uses consistent and well-matched $M_{\rm BH}$ distributions, and can robustly probe the expected change in AGN SEDs as a function of $L_{\rm bol}/L_{\rm Edd}$. We note that the excellent match in $M_{\rm BH}$ distribution between the XMM-COSMOS broad-line AGN and our changing-look quasars is the reason we specifically use XMM-COSMOS AGN instead of results from other previous investigations of the relation between $\alpha_{\rm OX}$ and $L_{\rm bol}/L_{\rm Edd}$ in luminous quasars[65–73].

Alternative models of X-ray binary state transitions

The analogous accretion flow structure of X-ray binaries and AGN implied by their similar spectral evolution also enables us to apply alternative models of X-ray binary accretion state transitions to describe AGN phenomenology, aside from the truncated disc model shown in Fig. 3. In particular, recent observations of X-ray binaries have suggested that the thin accretion disc might not experience large-scale truncation during the transition from the high/soft state to the low/hard state[74–76]. Alternative models of X-ray binary accretion state transitions propose that the inner radius of the thin disc remains within a few gravitational radii of the innermost stable circular orbit, even in the low/hard state[77–79]. In a subset of these models, the observed spectral evolution during transitions from high/soft state to the low/hard state is attributed to a decrease in the apparent temperature of the emergent thin disc spectrum, which causes a spectral hardening due to a more prominent coronal spectral component[80]. This evolution of the emergent thin disc spectrum may be due to the detailed radiative transfer in the photosphere of the thin disc during a transition to the low/hard state[81–84], and does not involve large-scale truncation of the inner disc radius.

Supplementary Figure 9 illustrates an application of such a disc spectral evolution model for X-ray binary accretions state transitions, to explain AGN phenomenology. In the high/soft state ($10^{-1} \lesssim L_{\rm bol}/L_{\rm Edd} \lesssim 1$), AGN emit luminous UV emission from a thin disc that extends close to the innermost stable circular orbit, which results in soft $\alpha_{\rm OX}$. This geometry is similar to the high/soft states in truncated disc models. However, as the accretion rate drops towards $L_{\rm bol}/L_{\rm Edd} \sim 10^{-2}$ and the AGN enters the low/hard state, the inner radius of the disc does not experience large-scale truncation. Instead, the luminosity fades due to a decrease in the apparent disc temperature, and the $\alpha_{\rm OX}$ hardens owing to a more prominent coronal component. At this point, the corona may become vertically extended as suggest by

observations of an increase in the coronal variability timescales[85]. At the lowest Eddington ratios ($L_{\rm bol}/L_{\rm Edd} \lesssim 10^{-2}$), large-scale truncation of the disc is still likely to occur as suggested by observations of X-ray binaries at low luminosities[86–90]. Thus, the spectral softening in this regime still likely owes to synchrotron emission from a jet[29,78] or the advection dominated accretion flow[91].

Data availability All data necessary to reproduce the results (including observations from *Chandra*, *ROSAT*, *XMM-Newton*, and SDSS) are publicly available online. All derived properties from the reduced data that are used in our analysis are available in the main text or the supplementary information.

Additional References

31. Bennett, C. L., Larson, D., Weiland, J. L. & Hinshaw, G. The 1% Concordance Hubble Constant. *Astrophys. J.* **794**, 135 (2014).
32. Fruscione, A. *et al.* CIAO: Chandra's data analysis system. *Proc. SPIE* **6270**, 62701V (2006).
33. Gu, M. & Cao, X. The anticorrelation between the hard X-ray photon index and the Eddington ratio in low-luminosity active galactic nuclei. *Mon. Not. R. Astron. Soc.* **399**, 349-356 (2009).
34. Constantin, A. *et al.* Probing the Balance of AGN and Star-forming Activity in the Local Universe with ChaMP. *Astrophys. J.* **705**, 1336-1355 (2009).
35. Younes, G., Porquet, D., Sabra, S. & Reeves, J. N. Study of LINER sources with broad Hα emission. X-ray properties and comparison to luminous AGN and X-ray binaries. *Astron. Astrophys.* **530**, A149 (2011).
36. Dickey, J. M. & Lockman, F. J. H I in the Galaxy. *Annu. Rev. Astron. Astrophys* **28**, 215-261 (1990).
37. Verner, D. A., Ferland, G. J., Korista, K. T. & Yakovlev, D. G. Atomic Data for Astrophysics. II. New Analytic FITS for Photoionization Cross Sections of Atoms and Ions. *Astrophys. J.* **465**, 487 (1996).
38. Wilms, J., Allen, A. & McCray, R. On the Absorption of X-Rays in the Interstellar Medium. *Astrophys. J.* **542**, 914-924 (2000).
39. IRAF is distributed by the National Optical Astronomy Observatory, which is operated by the Association of Universities for Research in Astronomy (AURA) under a cooperative agreement with the National Science Foundation.
40. Schlegel, D. J., Finkbeiner, D. P. & Davis, M. Maps of Dust Infrared Emission for Use in Estimation of Reddening and Cosmic Microwave Background Radiation Foregrounds. *Astrophys. J.* **500**, 525-553 (1998).
41. Cardelli, J. A., Clayton, G. C. & Mathis, J. S. The relationship between infrared, optical, and ultraviolet extinction. *Astrophys. J.* **345**, 245-256 (1989).
42. Voges, W. *et al.* The ROSAT all-sky survey bright source catalogue. *Astron. Astrophys.* **349**, 389-405 (1999).
43. York, D. G. *et al.* The Sloan Digital Sky Survey: Technical Summary. *Astron. J.* **120**, 1579-1587 (2000).
44. Vanden Berk, D. E. *et al.* Spectral Decomposition of Broad-Line AGNs and Host Galaxies. *Astron. J.* **131**, 84-99 (2006).
45. Shen, Y. *et al.* The Sloan Digital Sky Survey Reverberation Mapping Project: No Evidence for Evolution in the $M - \sigma$ Relation to $z \sim 1$. *Astrophys. J.* **805**, 96 (2015).
46. Yip, C. W. *et al.* Spectral Classification of Quasars in the Sloan Digital Sky Survey: Eigenspectra, Redshift, and Luminosity Effects. *Astron. J.* **128**, 2603-2630 (2004).
47. Yip, C. W. *et al.* Distributions of Galaxy Spectral Types in the Sloan Digital Sky Survey, Redshift, and Luminosity Effects. *Astron. J.* **128**, 585-609 (2004).
48. Vanden Berk, D. E. *et al.* Composite Quasar Spectra from the Sloan Digital Sky Survey. *Astron. J.* **122**, 549-564 (2001).
49. Boroson, T. A. & Green, R. F. The emission-line properties of low-redshift quasi-stellar objects. *Astrophys. J. Supp.* **80**, 109-135 (1992).
50. Grandi, S. A. The 3000 A bump in quasars. *Astrophys. J.* **255**, 25-38 (1982).
51. Wills, B. J., Netzer, H. & Wills, D. Broad emission features in QSOs and active galactic nuclei. II - New observations and theory of Fe II and H I emission. *Astrophys. J.* **288**, 94-116 (1985).
52. Storey, P. J. & Hummer, D. G. Recombination line intensities for hydrogenic ions-IV. Total recombination coefficients and machine-readable tables for Z=1 to 8. *Mon. Not. R. Astron. Soc.* **272**, 41-48 (1995).
53. Tananbaum, H. *et al.* X-ray studies of quasars with the Einstein Observatory.. *Astrophys. J.* **234**, L9-L13 (1979).
54. Greene, J. E., Peng, C. Y. & Ludwig, R. R. Redshift Evolution in Black Hole-Bulge Relations: Testing C IV-Based Black Hole Masses. *Astrophys. J.* **709**, 937-949 (2010).
55. Bentz, M. C. *et al.* Redshift Evolution in Black Hole-Bulge Relations: Testing C IV-Based Black Hole Masses. *Astrophys. J.* **697**, 160-181 (2009).
56. Vestergaard, M. & Peterson, B. M. Determining Central Black Hole Masses in Distant Active Galaxies and Quasars. II. Improved Optical and UV Scaling Relationships. *Astrophys. J.* **641**, 689-709 (2006).
57. Lusso, E. *et al.* Bolometric luminosities and Eddington ratios of X-ray selected active galactic nuclei in the XMM-COSMOS survey. *Mon. Not. R. Astron. Soc.* **425**, 623-640 (2012).
58. Runnoe, J. C. *et al.* Updating quasar bolometric luminosity corrections. *Mon. Not. R. Astron. Soc.* **422**, 478-493 (2012).
59. Vasudevan, R. V. & Fabian, A. C. Piercing Together the X-ray Background: Bolometric Corrections for Active Galactic Nuceli. *Mon. Not. R. Astron. Soc.* **381**, 1235-1251 (2007).
60. Vasudevan, R. V. & Fabian, A. C. Simultaneous X-ray/optical/UV snapshots of active galactic nuclei from XMM-Newton: spectral energy distributions for the reverberation mapped sample. *Mon. Not. R. Astron. Soc.* **392**, 1124-1140 (2009).
61. Mitsuda, K. *et al.* Energy spectra of low-mass binary X-ray sources observed from TENMA. *PASJ* **36**, 741-759 (1984).
62. Zdziarski, A. A., Johnson, W. N. & Magdziarz, P. Broad-band Gamma-ray and X-ray spectra of NGC 4151 and their implications for physical processes and geometry. *Mon. Not. R. Astron. Soc.* **283**, 193-206 (1996).
63. Coppi, P. S., The Physics of Hybrid Thermal/Non-Thermal Plasmas. ASP Conference Series 161, 375 1999,
64. Gierliński, M. *et al.* Radiation mechanisms and geometry of Cygnus X-1 in the soft state. *Mon. Not. R. Astron. Soc.* **309**, 496-512 (1999).
65. Vignali, C., Brandt, W. N. & Schneider, D. P. X-Ray Emission from Radio-Quiet Quasars in the Sloan Digital Sky Survey Early Data Release: The $\alpha_{\rm OX}$ Dependence upon Ultraviolet Luminosity. *Astron. J.* **125**, 433-443 (2003).
66. Strateva, I. V., Brandt, W. N., Schneider, D. P., Vanden Berk, D. G. & Vignali, C. Soft X-Ray and Ultraviolet Emission Relations in Optically Selected AGN Sample. *Astron. J.* **130**, 387-405 (2005).
67. Steffen, A. T. *et al.* The X-Ray-to-Optical Properties of Optically Selected Active Galaxies over Wide Luminosity and Redshift Ranges. *Astron. J.* **131**, 2826-2842 (2006).
68. Just, D. W. *et al.* The X-Ray Properties of the Most Luminous Quasars from the Sloan Digital Sky Survey. *Astrophys. J.* **665**, 1004-1022 (2007).
69. Grupe, D., Komossa, S., Leighly, K. M. & Page, K. L. The Simultaneous Optical-to-X-Ray Spectral Energy Distribution of Soft X-Ray Selected Active Galactic Nuclei Observed by Swift. *Astrophys. J. Supp.* **187**, 64-106 (2010).
70. Jin, C., Done, C. & Ward, M. A combined optical and X-ray study of unobscured type 1 active galactic nuclei - III. Broad-band SED properties. *Mon. Not. R. Astron. Soc.* **420**, 1825-1847 (2012).
71. Wu, J. *et al.* A Quasar Catalog with Simultaneous UV, Optical, and X-Ray Observations by Swift. *Astrophys. J.* **201**, 10 (2012).
72. Vagnetti, F., Antonucci, M. & Trevese, D. Variability and the X-ray/UV ratio of active galactic nuclei. II. Analysis of a low-redshift Swift sample. *Astron. Astrophys.* **550**, A71 (2013).
73. Trichas, M. *et al.* Empirical Links between XRB and AGN Accretion Using the Complete z $<$ 0.4 Spectroscopic CSC/SDSS Catalog. *Astrophys. J.* **778**, 188 (2013).
74. Reis, R. C., Fabian, A. C. & Miller, J. M. Black hole accretion discs in the canonical low-hard state. *Mon. Not. R. Astron. Soc.* **402**, 836-854 (2010).
75. Dunn, R. J. H., Fender, R. P., Merloni, A. & Körding, E. G. A global study of the behaviour of black hole X-ray binary discs. *Mon. Not. R. Astron. Soc.* **411**, 337-348 (2011).
76. Reynolds, M. T. & Miller, J. M. A Swift Survey of Accretion onto Stellar-mass Black Holes. *Astrophys. J.* **769**, 16 (2013).
77. Beloborodov, A. M. Plasma Ejection from Magnetic Flares and the X-Ray Spectrum of Cygnus X-1. *Astrophys. J.* **510**, L123-L126 (1999).
78. Markoff, S., Falcke, H. & Fender, R. A jet model for the broadband spectrum of XTE J1118+480. Synchrotron emission from radio to X-rays in the Low/Hard spectral state. *Astron. Astrophys.* **372**, L25-L28 (2001).
79. Merloni, A. & Fabian, A. C. A Coronal outflow dominated accretion discs: a new possibility for low-luminosity black holes?. *Mon. Not. R. Astron. Soc.* **332**, 165-175 (2002).

80. Salvesen, G., Miller, J. M., Begelman, M. C. & Reis, R. C. Spectral hardening as a viable alternative to disc truncation in black hole state transitions. *Mon. Not. R. Astron. Soc.* **431**, 3510-3532 (2013).
81. Shimura, T. & Takahara, F. On the spectral hardening factor of the X-ray emission from accretion discs in black hole candidates. *Astrophys. J.* **445**, 780-788 (1995).
82. Merloni, A., Fabian, A. C. & Ross, R. R. On the interpretation of the multicolour disc model for black hole candidates. *Mon. Not. R. Astron. Soc.* **313**, 193-197 (2000).
83. Davis, S. W., Blaes, O. .M, Hubeny, I. & Turner, N. J. Relativistic Accretion disc Models of High-State Black Hole X-Ray Binary Spectra. *Astrophys. J.* **621**, 372-387 (2005).
84. Davis, S. W., & Samer, E Spectral Hardening in Black Hole Accretion: Giving Spectral Modelers an f. https://arxiv.org/abs/1809.05134 (2018).
85. Kara, E. *et al.* The corona contracts in a new black hole transient. *Nature* **565**, 198-201 (2019).
86. Tomsick, J. A. *et al.* Truncation of the Inner Accretion disc Around a Black Hole at Low Luminosity. *Astrophys. J.* **707**, L87-L91 (2009).
87. Plant, D. S., Fender, R. .P, Muñoz-Darias, T. & Coriat, M. The truncated and evolving inner accretion disc of the black hole GX 339-4. *Astron. Astrophys.* **573**, A120 (2015).
88. Basak, R. & Zdziarski, A. A. Spectral analysis of the XMM-Newton data of GX 339-4 in the low/hard state: disc truncation and reflection. *Mon. Not. R. Astron. Soc.* **458**, 2199-2214 (2016).
89. Wang-Ji, J. *et al.* The Evolution of GX 339-4 in the Low-hard State as Seen by NuSTAR and Swift. *Astrophys. J.* **855**, 16 (2018).
90. van den Eijnden, J. *et al.* The very faint X-ray binary IGR J17062-6143: a truncated disc, no pulsations, and a possible outflow. *Mon. Not. R. Astron. Soc.* **475**, 2027-2044 (2018).
91. Wardziński, G. & Zdziarski, A. A. Thermal synchrotron radiation and its Comptonization in compact X-ray sources. *Mon. Not. R. Astron. Soc.* **314**, 183-198 (2000).

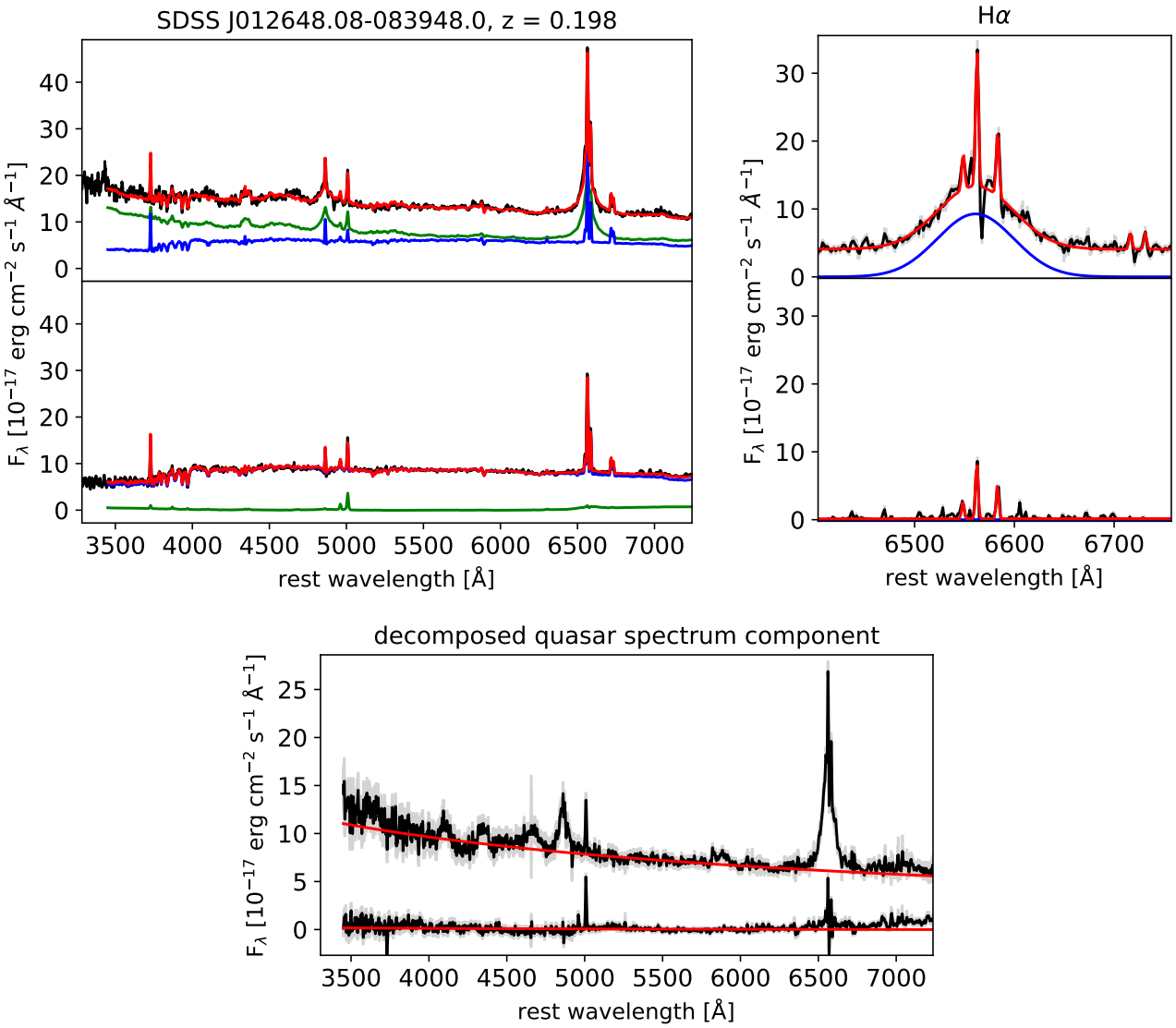

Supplementary Figure 1: **Spectral decomposition, broad-line fitting, and continuum fitting of SDSS spectra of the changing-look quasar J0126**. In the top left figure, the observed SDSS spectra of J0126 are shown (black) during the bright state (top panel) and during its faint state (bottom panel). The best-fit quasar components (green) and host galaxy components (blue) from our spectral decomposition are also shown, along with their sum (red). The top right figure shows our spectral fitting of the Hα region of the decomposed quasar component (black) in the bright state before its fading (top) and in the faint state after its fading (bottom). The best-fit broad Hα emission line (blue) and full spectral model (red) are also shown. The bottom figure shows our spectral fits to the continuum emission in the decomposed quasar component (black) in both the bright and faint states. The best-fit power-law continuum (red) and the 1σ observational uncertainties (grey) are also shown.

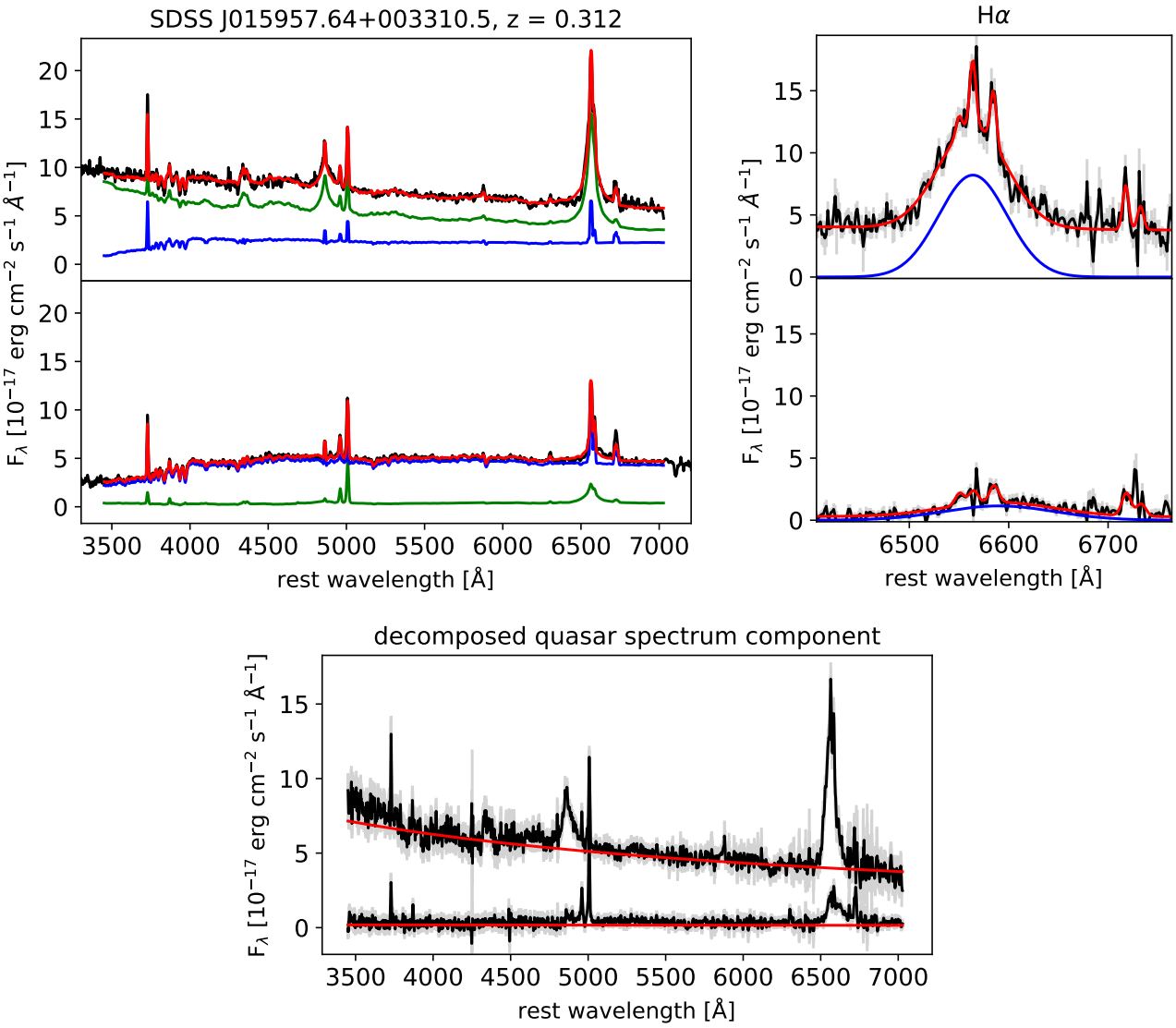

Supplementary Figure 2: Similar to Supplementary Fig. 1, but for J0159.

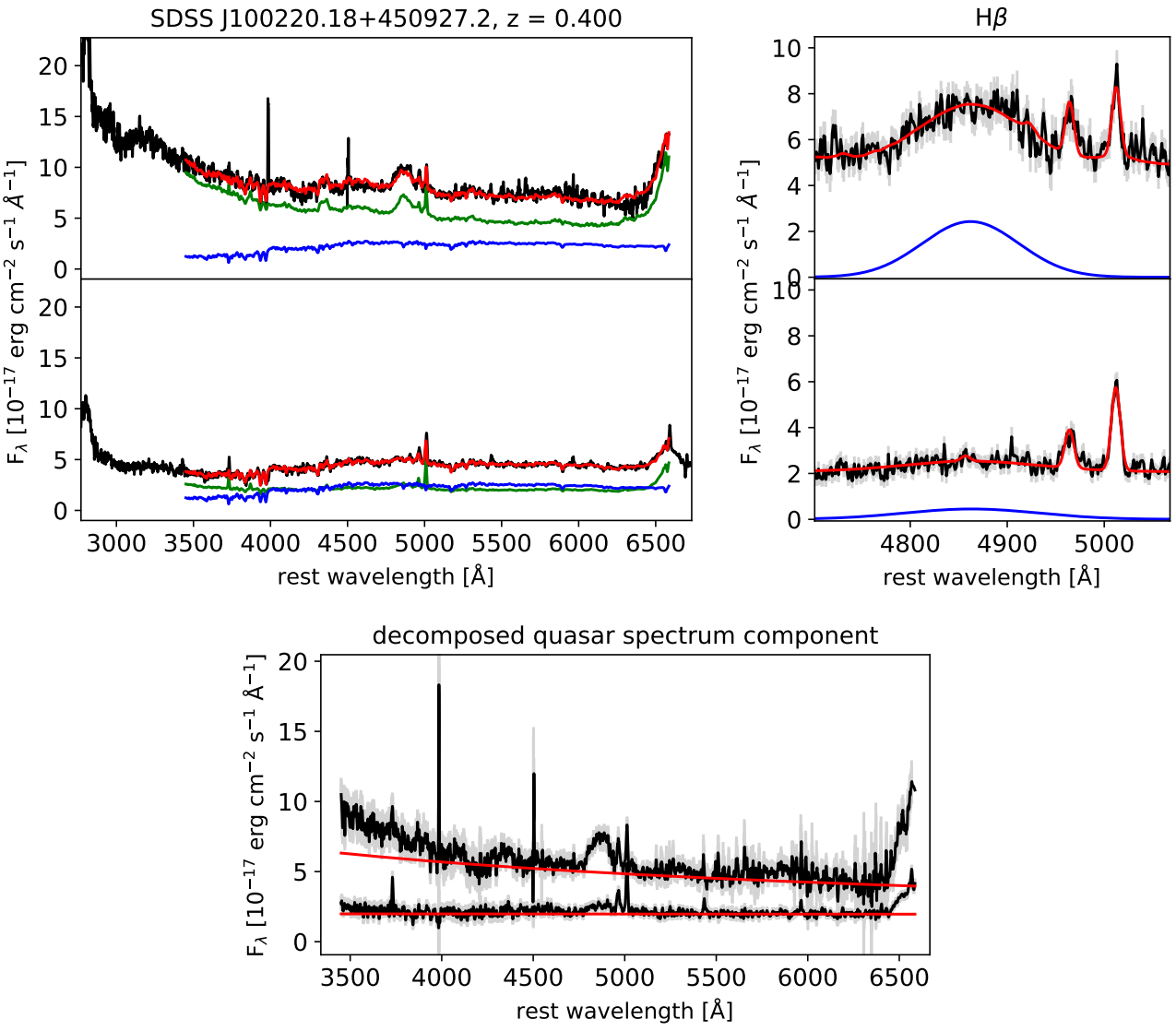

Supplementary Figure 3: Similar to Supplementary Fig. 1, but for J1002.

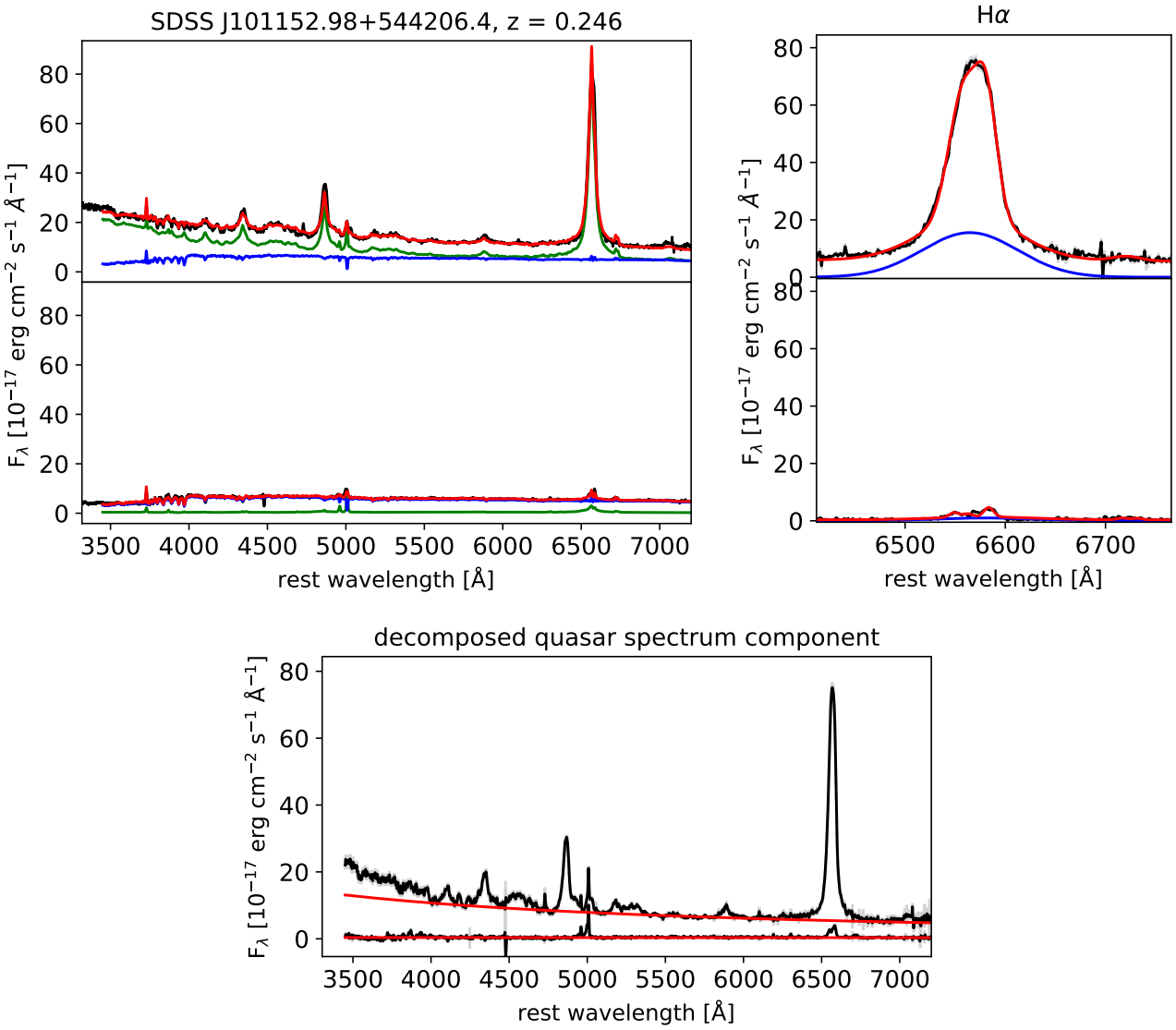

Supplementary Figure 4: Similar to Supplementary Fig. 1, but for J1011.

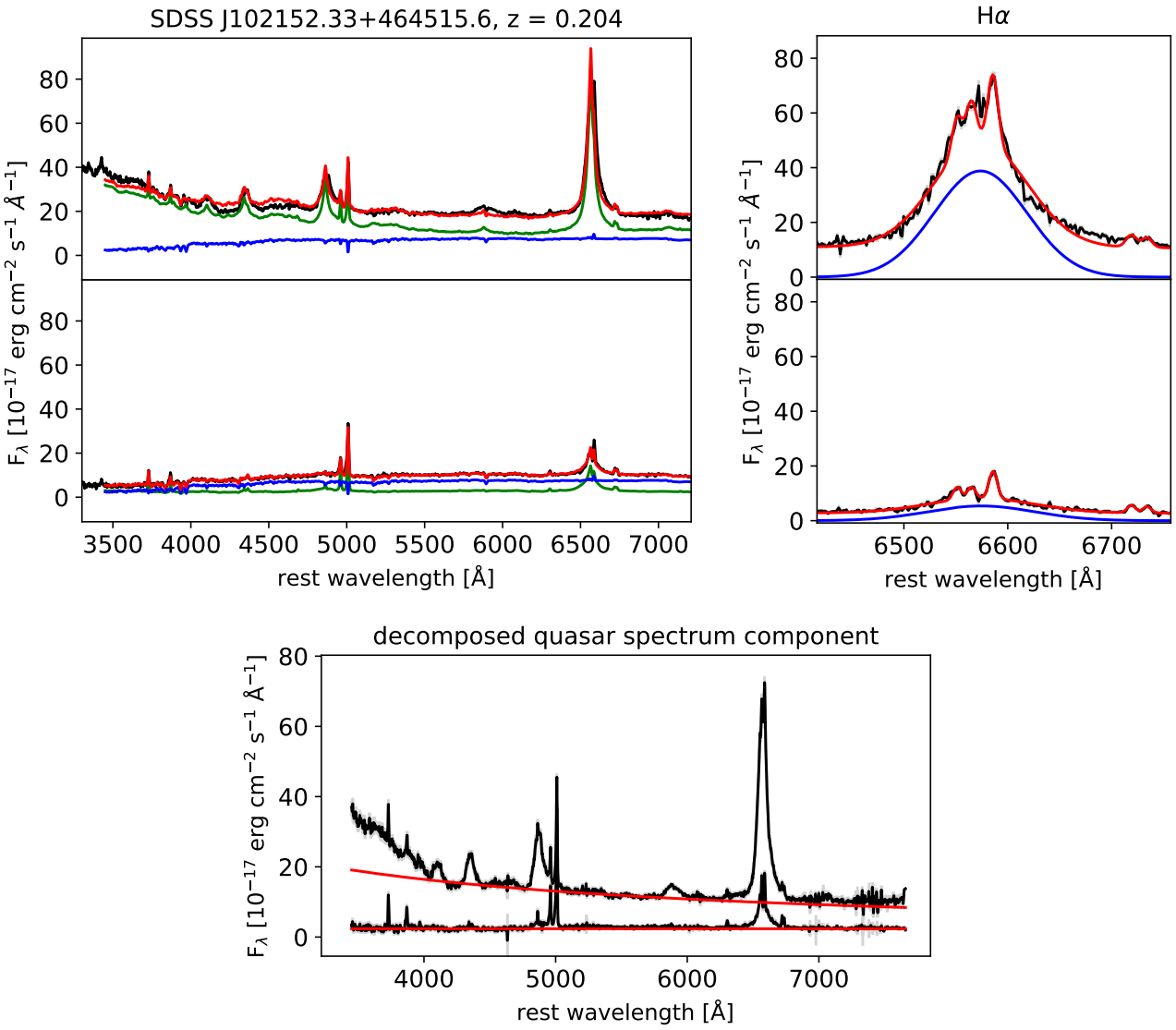

Supplementary Figure 5: Similar to Supplementary Fig. 1, but for J1021.

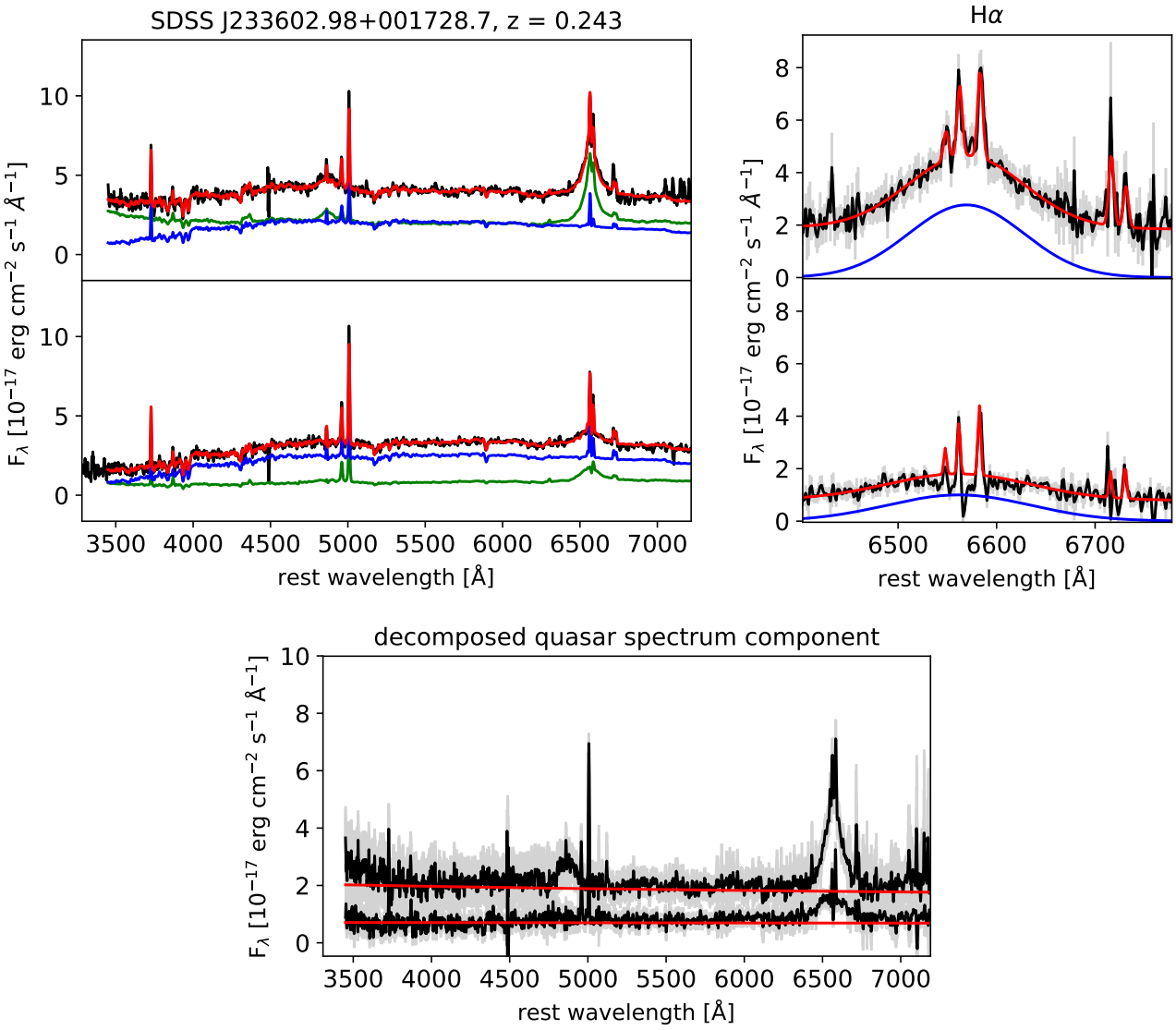

Supplementary Figure 6: Similar to Supplementary Fig. 1, but for J2336.

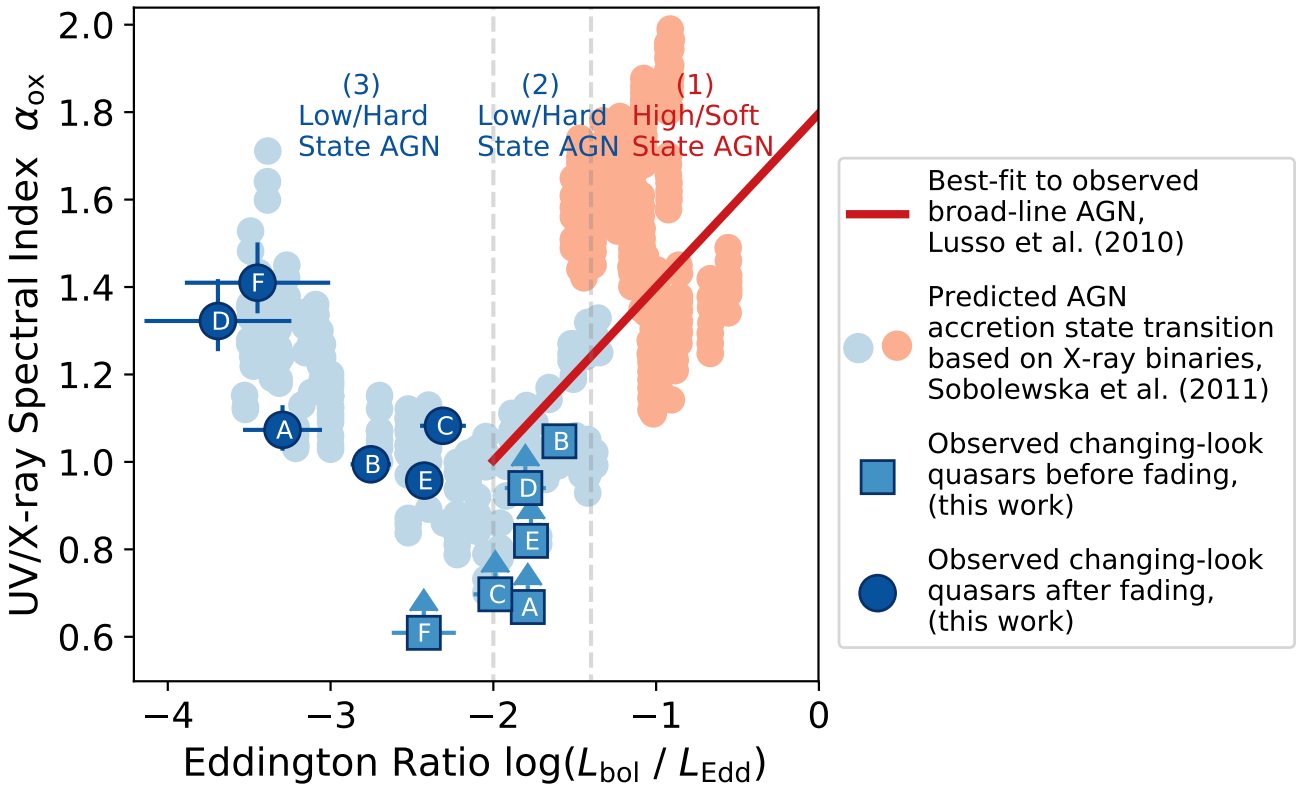

Supplementary Figure 7: **The observed α_{OX} behaviour of AGN as a function of Eddington ratio, calculated using $\lambda L_{3500\text{Å}}$.** This figure is exactly the same as Fig. 2, except that we have used the observed $\lambda L_{3500\text{Å}}$ to calculate α_{OX} for the changing-look quasars, instead of the extrapolated $\lambda L_{2500\text{Å}}$. The softening of α_{OX} at $L_{bol}/L_{Edd} \lesssim 10^{-2}$ is still clearly observed, and observations are still an excellent match to predictions from X-ray binary transitions. This demonstrates that our results are not strongly dependent on our extrapolation of the power-law continuum in the optical spectra to 2500 Å.

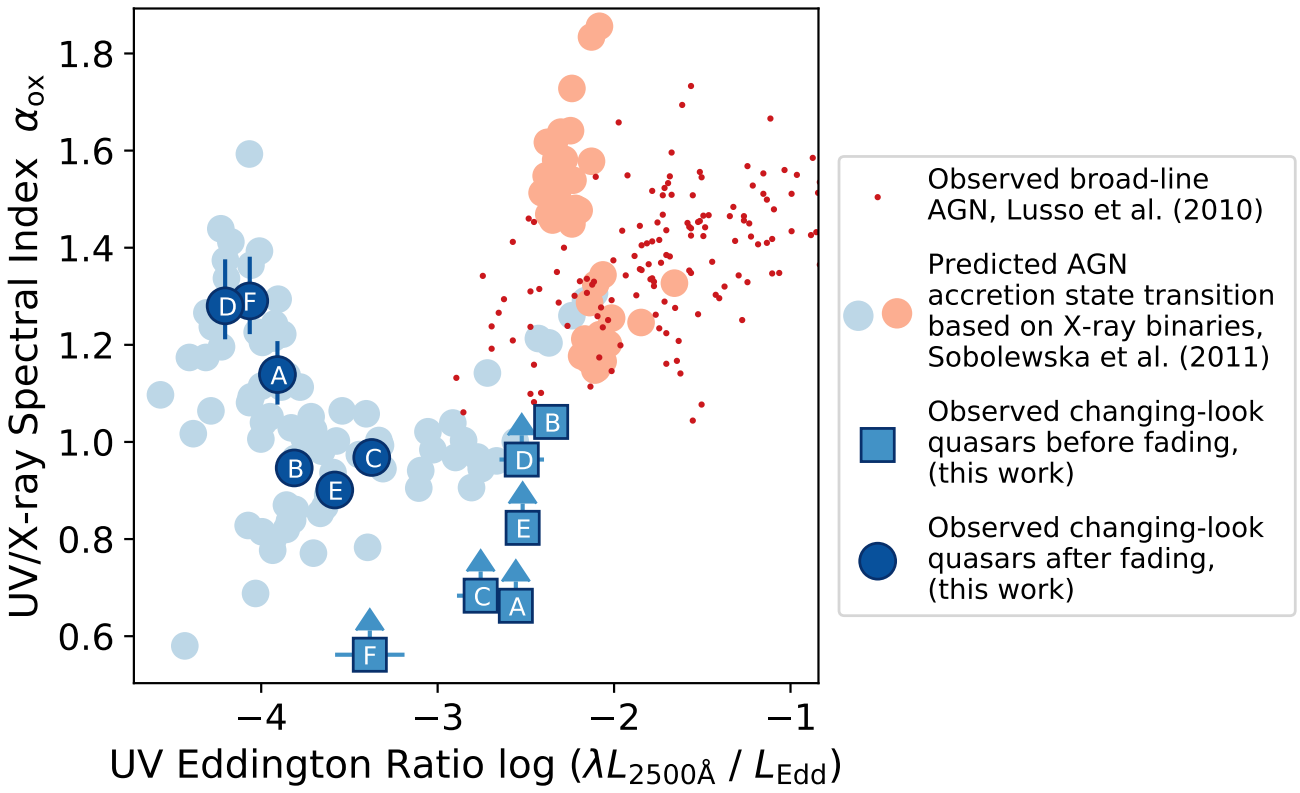

Supplementary Figure 8: **The observed α_{OX} behaviour of AGN as a function of UV Eddington ratio.** This figure is similar to Fig. 2, except that we show the UV Eddington ratio, which is based on the UV luminosity rather than the bolometric luminosity (i.e., we do not make a bolometric correction). The inflection in α_{OX} is still clearly observed, and observations are still an excellent match to predictions from X-ray binary transitions. This demonstrates that our results are not strongly dependent on the bolometric corrections we use.

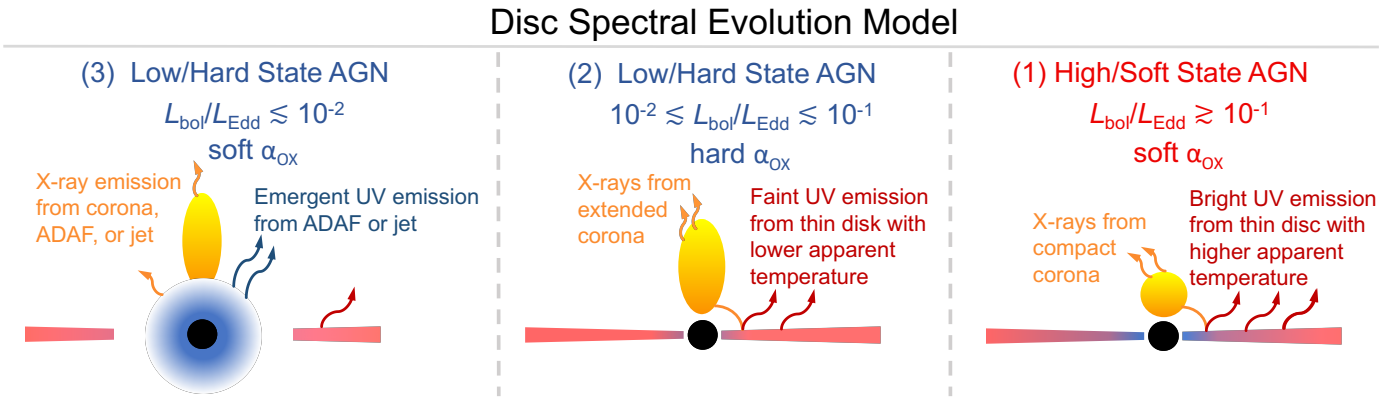

Supplementary Figure 9: **A alternative model for the geometry of AGN accretion flows in different accretion states.** The panels illustrate the application of a model in which the thin disc does not truncate, but rather the emergent disc spectrum decreases in temperature during the transition from the high/soft state to the low/hard state. The panels display the accretion flow geometry over ranges in Eddington ratio that correspond to those labeled in Fig. 2. Right panel: At high accretion rates ($L_{\rm bol}/L_{\rm Edd} \gtrsim 10^{-1}$) in the high/soft state, the soft $\alpha_{\rm OX}$ is due to bright UV emission from a thin accretion disc. Centre panel: As the accretion rate drops ($10^{-2} \lesssim L_{\rm bol}/L_{\rm Edd} \lesssim 10^{-1}$), the inner regions of the thin disc remains near the innermost stable circular orbit, but the apparent temperature of the emergent thin disc spectrum decreases. The increasing prominence of the coronal component thus causes $\alpha_{\rm OX}$ to harden. Left panel: At low accretion rates ($L_{\rm bol}/L_{\rm Edd} \lesssim 10^{-2}$), the $\alpha_{\rm OX}$ softens again due to the emergence of UV emission from either an advection dominated accretion flow or a jet.

Supplementary Table 1: **SDSS spectroscopic properties of changing-look quasars in both their bright and faint states.** Columns include the object name, redshift, observation date of each SDSS spectrum, the optical luminosity state of the changing-look quasar revealed by the SDSS spectrum, the measured broad emission line FWHM (from Hβ or Hα), and the derived black hole mass. All uncertainties are at 1σ c.l.

Object (SDSS)	z	Observation Date [MJD]	Luminosity State	$\log(\lambda L_{5100\mathring{\mathrm{A}}})$ [erg s^{-1}]	Broad Line FWHM [km s^{-1}]	$M_{\rm BH}$ [10^8 $M_\odot$]
J0126−0839	0.198	52163	bright	43.7±0.1	4100±300[a]	1.2±0.2
		54465	faint	42.1±0.1		
J0159+0033	0.312	51871	bright	43.9±0.1	3800±200[a]	1.4±0.2
		54465	faint	42.7±0.1		
J1002+4509	0.400	52376	bright	44.1±0.1	7300±1100[b]	5.0±1.5
		54465	faint	43.8±0.1		
J1011+5442	0.246	52652	bright	43.9±0.1	5200±600[a]	2.5±0.7
		54465	faint	42.6±0.1		
J1021+4645	0.204	52614	bright	43.9±0.1	4800±300[a]	2.1±0.3
		54465	faint	43.2±0.1		
J2336+0017	0.243	52096	bright	43.3±0.1	6300±800[a]	1.8±0.5
		54465	faint	42.8±0.1		

[a] Broad Hα emission; [b] Broad Hβ emission.

Supplementary Table 2: **APO spectroscopic observations of changing-look quasars.** Columns include the object name, observation date of the APO spectrum, exposure time, airmass, seeing, and the star used for spectrophotometric calibration.

Object (SDSS)	Observation Date [MJD]	Exposure Time [s]	Airmass	Seeing [arcsec]	Calibration Star
J0126−0839	58084	5×600	1.35	1.2	BD+28 4211
J0159+0033	58084	5×600	1.25	1.2	BD+28 4211
J1002+4509	58217	5×900	1.03	1.6	Feige 34
J1011+5442	58217	5×900	1.09	1.6	Feige 34
J1021+4645	57781	3×900	1.12	1.5	Feige 34
J2336+0017	58079	5×600	1.27	1.2	BD+28 4211

Supplementary Table 3: *Chandra* **X-ray properties of changing-look quasars in their current faint state.** Columns include the object name, observation date, the *Chandra* ObsID of the exposure, exposure time, count rate, and unabsorbed model flux. All uncertainties are at 1σ c.l.

Object (SDSS)	Observation Date [MJD]	Chandra ObsID	Exposure Time [ks]	Count Rate (0.5 - 7 keV) [10^{-3} cts s^{-1}]	Unabsorbed Flux (0.5 - 7 keV) [10^{-14} erg s^{-1} cm^{-2}]
J0126−0839	57978	19516	6.9	$1.8^{+0.6}_{-0.5}$	$2.0^{+0.7}_{-0.5}$
J0159+0033	57640	18639	20.7	$3.2^{+0.4}_{-0.4}$	$3.2^{+0.4}_{-0.4}$
J1002+4509	58131	19515	32.6	$15.0^{+0.8}_{-0.7}$	$16.6^{+0.8}_{-0.8}$
J1011+5442	58180	19518	10.9	$0.5^{+0.3}_{-0.2}$	$0.6^{+0.3}_{-0.2}$
J1021+4645	58049	19514	6.9	$26.5^{+0.2}_{-0.2}$	$28.6^{+2.3}_{-2.2}$
J2336+0017	57958	19517	10.9	$0.5^{+0.3}_{-0.2}$	$0.6^{+0.3}_{-0.2}$

Supplementary Table 4: *ROSAT* **and** *XMM-Newton* **X-ray properties of changing-look quasars in their former bright state.** Columns include the object name, observation date of the X-ray observation, the telescope used for the observation, exposure time, count rate, and unabsorbed model flux. All uncertainties are at 1σ c.l., and upper limits are 3σ.

Object (SDSS)	Observation Date [MJD]	Telescope	Exposure Time [ks]	X-ray Count Rate [10^{-1} cts s^{-1}]	Unabsorbed X-ray Flux [10^{-14} erg s^{-1} cm^{-2}]
J0126−0839	48083	ROSAT	0.4	$<3.5^{a}$	$<7.5^{a}$
J0159+0033	51732	XMM	10	0.2^{b}	$26.4^{+1.4\,b}_{-1.6}$
J1002+4509	48191	ROSAT	0.5	$< 4.0^{a}$	$<1.4^{a}$
J1011+5442	48177	ROSAT	0.5	$< 1.1^{a}$	$<0.45^{a}$
J1021+4645	48167	ROSAT	0.5	$< 4.2^{a}$	$<4.7^{a}$
J2336+0017	48224	ROSAT	0.4	$< 1.6^{a}$	$<3.5^{a}$

[a] 0.1 - 2.4 keV 3σ limit; [b] 2 - 10 keV

Supplementary Table 5: **Derived spectral properties of changing-look quasars in both their bright and faint states.** Columns include the object name, the optical luminosity state of the changing-look quasar revealed by the SDSS spectrum, bolometric Eddington ratio, UV-to-X-ray spectral index, X-ray luminosity, and UV luminosity. All uncertainties are at 1σ c.l., and upper/lower limits are 3σ.

Object (SDSS)	Luminosity State	$\log(L_{\rm bol}/L_{\rm Edd})$	$\alpha_{\rm OX}$	$\log(\nu L_{\rm 2keV})$ [erg s^{-1}]	$\log(\lambda L_{2500\mathring{\rm A}})$ [erg s^{-1}]
J0126−0839	bright	$-1.8^{+0.1}_{-0.1}$	$> 0.7^{\rm a}$	$< 44.5^{\rm a}$	43.6±0.1
	faint	$-3.2^{+0.3}_{-0.3}$	$1.1^{+0.1}_{-0.1}$	$41.9^{+0.1}_{-0.1}$	42.3±0.1
J0159+0033	bright	$-1.6^{+0.1}_{-0.1}$	$1.0^{+0.1}_{-0.1}$	$43.8^{+0.1}_{-0.1}$	43.9±0.1
	faint	$-2.8^{+0.1}_{-0.1}$	$1.0^{+0.1}_{-0.1}$	$42.6^{+0.1}_{-0.1}$	42.4±0.1
J1002+4509	bright	$-2.0^{+0.1}_{-0.1}$	$> 0.7^{\rm a}$	$< 44.9^{\rm a}$	44.1±0.1
	faint	$-2.4^{+0.1}_{-0.1}$	$1.0^{+0.1}_{-0.1}$	$43.5^{+0.1}_{-0.1}$	43.5±0.1
J1011+5442	bright	$-1.8^{+0.1}_{-0.1}$	$> 1.0^{\rm a}$	$< 44.1^{\rm a}$	44.0±0.1
	faint	$-3.8^{+0.4}_{-0.4}$	$1.3^{+0.1}_{-0.1}$	$41.6^{+0.3}_{-0.2}$	42.3±0.1
J1021+4645	bright	$-1.8^{+0.1}_{-0.1}$	$> 0.8^{\rm a}$	$< 44.4^{\rm a}$	43.9±0.1
	faint	$-2.5^{+0.1}_{-0.1}$	$0.9^{+0.1}_{-0.1}$	$43.1^{+0.1}_{-0.1}$	42.8±0.1
J2336+0017	bright	$-2.4^{+0.2}_{-0.2}$	$> 0.6^{\rm a}$	$< 44.1^{\rm a}$	43.0±0.1
	faint	$-3.5^{+0.4}_{-0.4}$	$1.4^{+0.1}_{-0.1}$	$41.6^{+0.2}_{-0.2}$	42.5±0.1

[a] 3σ limit